The Astrophysical Journal, 939:1 (22pp), 2022 November 1 https://doi.org/10.3847/1538-4357/ac9475

A Strong Shock During a Nova Outburst: An Origin of Multiple Velocity Systems in Optical Spectra and of High-energy Emissions

Izumi Hachisu[1] and Mariko Kato[2]

[1] Department of Earth Science and Astronomy, College of Arts and Sciences, The University of Tokyo, 3-8-1 Komaba, Meguro-ku, Tokyo 153-8902, Japan
izumi.hachisu@outlook.jp

[2] Department of Astronomy, Keio University, Hiyoshi, Kouhoku-ku, Yokohama 223-8521, Japan

Received 2022 July 7; revised 2022 September 16; accepted 2022 September 21; published 2022 October 26

Abstract

We propose a theoretical explanation of absorption/emission line systems in classical novae based on a fully self-consistent nova explosion model. We found that a reverse shock is formed far outside the photosphere ($\gtrsim 10^{13}$ cm) because later-ejected mass with a faster velocity collides with earlier-ejected matter. Optically thick winds blow continuously at a rate of $\sim 10^{-4}\,M_\odot\ \mathrm{yr}^{-1}$ near the optical maximum, but its velocity decreases toward the optical maximum and increases afterward, so that the shock arises only after the optical maximum. The nova ejecta is divided by the shock into three parts, the outermost expanding gas (earliest wind before maximum), shocked shell, and inner fast wind, which respectively contribute to pre-maximum, principal, and diffuse-enhanced absorption/emission line systems. A large part of nova ejecta is eventually confined to the shocked shell. The appearance of the principal system is consistent with the emergence of a shock. This shock is strong enough to explain thermal hard X-ray emissions. The shocked layer has a high temperature of $kT_{\rm sh} \sim 1\ \mathrm{keV} \times ((v_{\rm wind} - v_{\rm shock})/1000\ \mathrm{km\ s^{-1}})^2 = 1\ \mathrm{keV} \times ((v_{\rm d} - v_{\rm p})/1000\ \mathrm{km\ s^{-1}})^2$, where $v_{\rm d} - v_{\rm p}$ is the velocity difference between the diffuse-enhanced ($v_{\rm d}$) and principal ($v_{\rm p}$) systems. We compare a 1.3 $M_\odot$ white dwarf model with the observational properties of the GeV gamma-ray detected classical nova V5856 Sgr (ASASSN-16ma) and discuss what kind of novae can produce GeV gamma-ray emissions.

Unified Astronomy Thesaurus concepts: Classical novae (251); High energy astrophysics (739); Cataclysmic variable stars (203); Shocks (2086); X-ray astronomy (1810); Gamma-ray astronomy (628); White dwarf stars (1799)

1. Introduction

One of the long-standing problems in novae is the origin of different velocity systems of absorption/emission lines in nova spectra. McLaughlin (1942) first classified nova spectra into three systems: (i) the pre-maximum, (ii) principal, and (iii) diffuse-enhanced absorption/emission line systems. The pre-maximum system is observed only in the pre-maximum phase and up to a few to several days after the maximum. The principal and diffuse-enhanced systems show different velocities, both increase with time (see Tables 3 and 5 of McLaughlin 1943). The principal system becomes dominant after the optical maximum. These multiple velocity systems indicate multiple mass ejections with different velocities. However, no theoretical work has explained such multiple mass ejections within the framework of one-dimensional (1D) approximation.

In the last decades, hard X-ray and GeV gamma-ray emissions have been observed in classical novae. Hard X-rays were detected in a middle phase of a nova outburst, i.e., from a few t_3 times to several t_3 times after the optical maximum (e.g., Lloyd et al. 1992; Balman et al. 1998; Mukai & Ishida 2001), where t_3 time is the 3 mag decay time from the optical peak. GeV gamma-ray emissions were observed in an early phase of a nova, from the post-maximum phase, and continues a few tens of days (e.g., Abdo et al. 2010; Ackermann et al. 2014; Li et al. 2017; Gordon et al. 2021).

These high-energy (hard X-rays and GeV gamma rays) emissions are considered to originate from strong shocks between shells ejected with different velocities (Chomiuk et al. 2014; Metzger et al. 2015; Martin et al. 2018). If the inner shell (later ejected) has a larger velocity than that of the outer shell (earlier ejected), the inner one can catch up with the outer one and forms a shock wave (e.g., Mukai & Sokoloski 2019; Aydi et al. 2020a, 2020b). The assumption of multiple shell ejections is the key of this idea.

In this way, multiple shell ejections were suggested from both optical and high-energy emissions from novae. There is, however, no unified theory that naturally explains all these different wavelength observations based on nova explosion models (see Chomiuk et al. 2021, for a recent review).

From the theoretical point of view, many numerical calculations have been presented from the early thermonuclear runaway to the extended phase of nova outbursts (e.g., Prialnik & Kovetz 1992, 1995; Epelstain et al. 2007; Starrfield et al. 2009; Denissenkov et al. 2013; Chen et al. 2019; Kato et al. 2022a, 2022b). These works clarified that mass ejection is continuous, and no multiple distinct mass ejections occur. Also no shock arises at the thermonuclear runaway (see Section 2.1 for more detail).

Thus, we have to bridge the gap between these theoretical understandings of continuous mass loss and distinct multiple mass ejections. The aim of this paper is to present a natural explanation for a shock formation during nova outburst and multiple velocities of ejecta based on our theoretical nova evolution models (Kato et al. 2022a).

This paper is organized as follows. First we summarize the current common understanding of a shock in nova theory

(Section 2.1). Then, we introduce our nova model in Section 2.2 and clarify that a shock is formed far outside the photosphere in Section 2.3. The origin of absorption/emission line systems is presented and discussed in Section 3. High-energy (hard X-rays and GeV gamma rays) emissions from a shock are separately discussed in Section 4. A discussion follows in Sections 5.1–5.8. Especially, we compare the present results with the observational properties of the classical nova V5856 Sgr (ASASSN-16ma) in Section 5.5. The conclusion follows in Section 6.

2. Shock Formation Outside the Photosphere

2.1. *Where is a Shock Arising?*

Nova outbursts have been studied since the 1970s by various authors. Among those people, Starrfield et al. (1972) calculated a strong shock associated with thermonuclear runaway. Prialnik (1986) wrote that a nova outburst experiences massive shock ejection. Prialnik & Kovetz (1992) later wrote "we find continuous mass loss instead of shock ejection. These differences may be the result of our more accurate treatment of mass loss." Since then, many numerical calculations have been presented (e.g., Prialnik & Kovetz 1995; Epelstain et al. 2007; Starrfield et al. 2009; Denissenkov et al. 2013; Chen et al. 2019), but no one detected a shock wave.

Kato et al. (2022a) explained why a shock wave does not arise around the nuclear burning region. The timescale of nuclear energy generation (∼100 s) is larger (longer) than the hydrodynamic timescale (∼0.4 s). A huge amount of nuclear energy is generated, which is once absorbed by the layer around nuclear burning region and then will be released in a later phase with a long timescale. During the nova outburst, the white dwarf (WD) envelope quickly expands to a giant size, but no shock arises below the photosphere (e.g., Denissenkov et al. 2013; Kato et al. 2022a, 2022b). Thus, the statement "no shock arises during/after thermonuclear runaway" is the current understanding in nova theory.

2.2. *A Self-consistent Nova Model*

Although no shock arises inside the photosphere, a shock could be generated *outside* the photosphere. Matter is ejected through the photosphere. Such matter has usually been removed from the code, mainly because of difficulty of calculation in Henyey-type codes (see, e.g., Kato et al. 2017a, for details).

In the present paper, we use the nova model calculated by Kato et al. (2022a). They obtained internal structure from the WD center to the photosphere, consistently including wind acceleration of radiation-pressure gradient (so-called optically thick wind). This model is for a $1.0\,M_\odot$ WD with the mass accretion rate to the WD before the outburst of $\dot{M}_{\rm acc} = 5 \times 10^{-9}\ M_\odot\ {\rm yr}^{-1}$, a typical parameter for classical novae. This is only the fully self-consistent model of classical nova calculation (see also Kato et al. 2017b, for another self-consistent model, but for recurrent novae of $1.2\ M_\odot$ and $1.38\ M_\odot$ WDs).

Figure 1(a) shows the photospheric radius and wind mass-loss rate of the nova outburst model mentioned above. The thermonuclear runaway starts at $t = 0$, and then the hydrogen-rich envelope begins to expand. The wind (optically thick wind) is accelerated at $t = 1.05$ day. The photospheric radius reaches the maximum value of $R_{\rm ph} \sim 5 \times 10^{12}$ cm ($\approx 71\,R_\odot$) at $t = 26$ day, where the photospheric temperature is $T_{\rm ph} \sim 8000$ K (not shown in Figure 1). The wind mass-loss rate also reaches the maximum, $\dot{M}_{\rm wind} \sim 1.4 \times 10^{-4}\ M_\odot\ {\rm yr}^{-1}$. After that, the photospheric radius decreases and the temperature increases with time because the envelope loses its mass owing to optically thick winds.

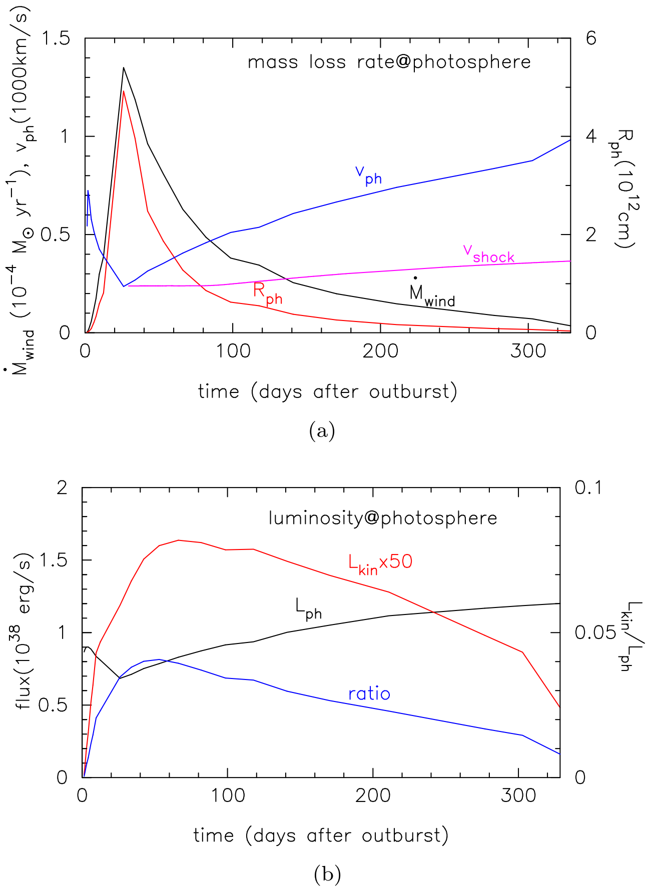

(a)

(b)

Figure 1. Various photospheric properties of a $1.0\ M_\odot$ WD model (Kato et al. 2022a). (a) The wind mass-loss rate (solid black line, labeled $\dot{M}_{\rm wind}$), wind velocity (blue, $v_{\rm ph}$), and photospheric radius (red, $R_{\rm ph}$) are plotted against time (days after outburst). We also add the shock velocity (magenta, $v_{\rm shock}$). The shock is located far outside the photosphere (see Figure 3(a) for the position of the shock). (b) The photospheric luminosity, $L_{\rm ph}$, is plotted against time (days after outburst). We also add the kinetic energy of the wind at the photosphere, $L_{\rm kin}$, which is multiplied by 50. The ratio of $L_{\rm kin}$ to $L_{\rm ph}$ is also plotted. The kinetic energy does not exceed 5% of the photospheric luminosity.

This figure also shows the velocity of outgoing matter at the photosphere. The velocity is smaller than a typical absorption line velocity of fast novae (1000–2000 km s^{-1}) but consistent with that of slow and very slow novae (200–800 km s^{-1}).[3] The velocity of wind $v_{\rm ph}$ decreases toward the optical maximum and then increases afterward (blue line in Figure 1(a)). This trend in the photospheric velocity $v_{\rm ph}$ is commonly observed in many novae. For example, Aydi et al. (2020a) showed temporal variations of the velocities in the Hα or Hβ P Cygni profiles of four novae, V906 Car, V435 CMa, V549 Vel, and V5855 Sgr in their Figure 11. Among the four novae, three novae, V906 Car, V435 CMa, and V5855 Sgr, show slow velocities of ∼200–250 km s^{-1} near the maximum, which are consistent with our model of $v_{\rm ph} \sim 235$ km s^{-1} at maximum expansion of the photosphere (see Figure 1(a)).

---

[3] The nova speed class is defined by t_3 or t_2 (days of 3 or 2 mag decay from the optical maximum). For example, very fast novae ($t_2 \leqslant 10$ day), fast novae ($11 \leqslant t_2 \leqslant 25$ day), moderately fast nova ($26 \leqslant t_2 \leqslant 80$ day), slow novae ($81 \leqslant t_2 \leqslant 150$ day), and very slow novae ($151 \leqslant t_2 \leqslant 250$ day), which are defined by Payne-Gaposchkin (1957).

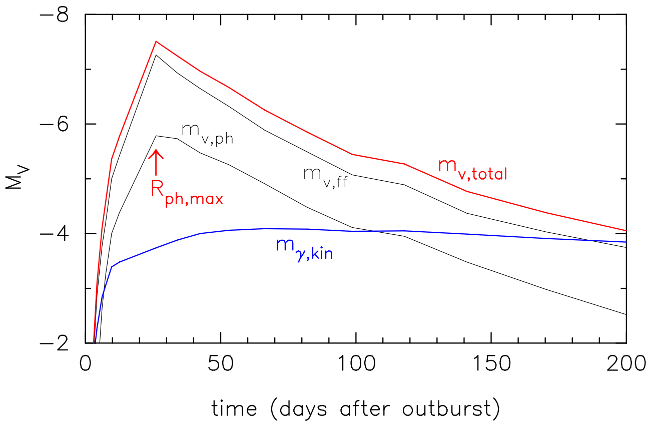

Figure 2. Three absolute V magnitudes, $m_{V,\rm total}$, $m_{V,\rm ff}$, and $m_{V,\rm ph}$ are plotted against time (days after outburst). The total V magnitude is the sum of the free–free emission component ($m_{V,\rm ff}$) and the photospheric blackbody component ($m_{V,\rm ph}$). The optical maximum in the $m_{V,\rm total}$ magnitude corresponds to the maximum expansion of the photosphere (labeled $R_{\rm ph,\,max}$). No circumstellar or interstellar extinctions are included. We also add the kinematic component (kinetic energy of wind) of $m_{\gamma,\rm kin}$. The three V magnitudes of $m_{V,\rm total}$, $m_{V,\rm ff}$, and $m_{V,\rm ph}$ are calibrated, where the distance $d = 10$ pc is assumed, but only the $m_{\gamma,\rm kin}$ magnitude is scale-free, not calibrated.

Figure 1(b) shows the temporal variations of the photospheric luminosity $L_{\rm ph}$, kinetic energy flux of wind $L_{\rm kin} \equiv \dot{M}_{\rm wind}\, v_{\rm ph}^2/2$, and the ratio of $L_{\rm kin}/L_{\rm ph}$. The photospheric luminosity decreases toward the optical maximum and increases after that. The optical (V band) maximum of this model corresponds to the maximum expansion of the photosphere and, at the same time, the maximum wind mass-loss rate (see Figure 2 for the V magnitude of this model, the details of which are presented in Section 5.1). This is due to the energy balance in the envelope in which a larger part of the diffusive luminosity is consumed to lift up the wind matter, so the photospheric luminosity is smaller when the mass-loss rate is larger (see Figure 13 of Kato et al. 2022a, for the energy balance in the nova envelope).

The kinetic energy flux of the wind reaches $L_{\rm kin} \approx 3.2 \times 10^{36}$ erg s^{-1} just in the post-maximum phase, about 5% of the photospheric luminosity at the optical maximum. This small kinetic energy comes from energy balance in the envelope, in which the wind is accelerated owing to the radiation-pressure gradient deep inside the photosphere. It should be noted that the radiative energy is consumed to lift up the massive wind, and the residual is not enough to accelerate the wind to much higher velocities (see Kato et al. 2022a).

Even if a strong shock is formed above (outside) the photosphere and all the kinetic energy flux is converted to the optical luminosity at the shock, the luminosity of shock may not be larger than a few percent of the photospheric luminosity. Therefore, it is not enough to explain the super-Eddington luminosity as long as Kato et al. (2022a)'s model is concerned.

2.3. Formation of A Strong Shock Outside the Photosphere

Figure 1(a) shows the velocity of the wind at the photosphere, which decreases before the maximum expansion of the photosphere (optical maximum) and increases after that. Assuming a ballistic motion of a fluid particle, i.e., the velocity of gas is constant outside the photosphere, we plot the trajectory of wind in Figure 3(a). Before the optical maximum, the photospheric velocity decreases with time, so each locus departs from the others. After the optical maximum, on the other hand, the trajectory of the wind converges, i.e., the wind ejected later catches up with the previously ejected matter. Thus, matter will be compressed, which causes a strong shock wave. This occurs after the optical maximum. The temporal variation in the shock velocity is shown by the solid magenta line in Figure 1(a).

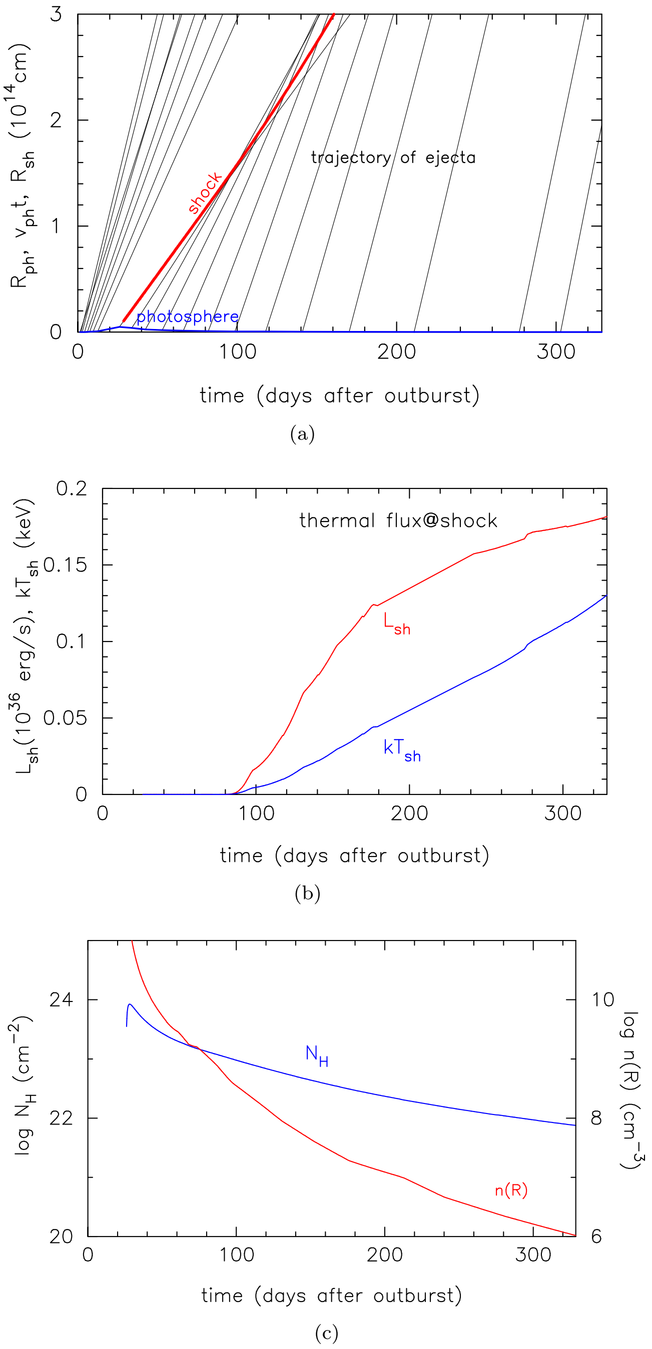

(a)

(b)

(c)

Figure 3. (a) Trajectories (thin black line) of the winds ejected from the model in Figure 1. We also add the position of the strong shock (thick red line). The thick blue line shows the position of the photosphere. (b) Temporal variation in the luminosity $L_{\rm sh}$ (solid red line) and temperature $kT_{\rm sh}$ (solid blue line) of shocked matter. (c) Temporal variation in the hydrogen column density $N_{\rm H}$ (blue line) behind the shock and the number density $n(R)$ (red line) just in front of the shock ($R = R_{\rm sh}$).

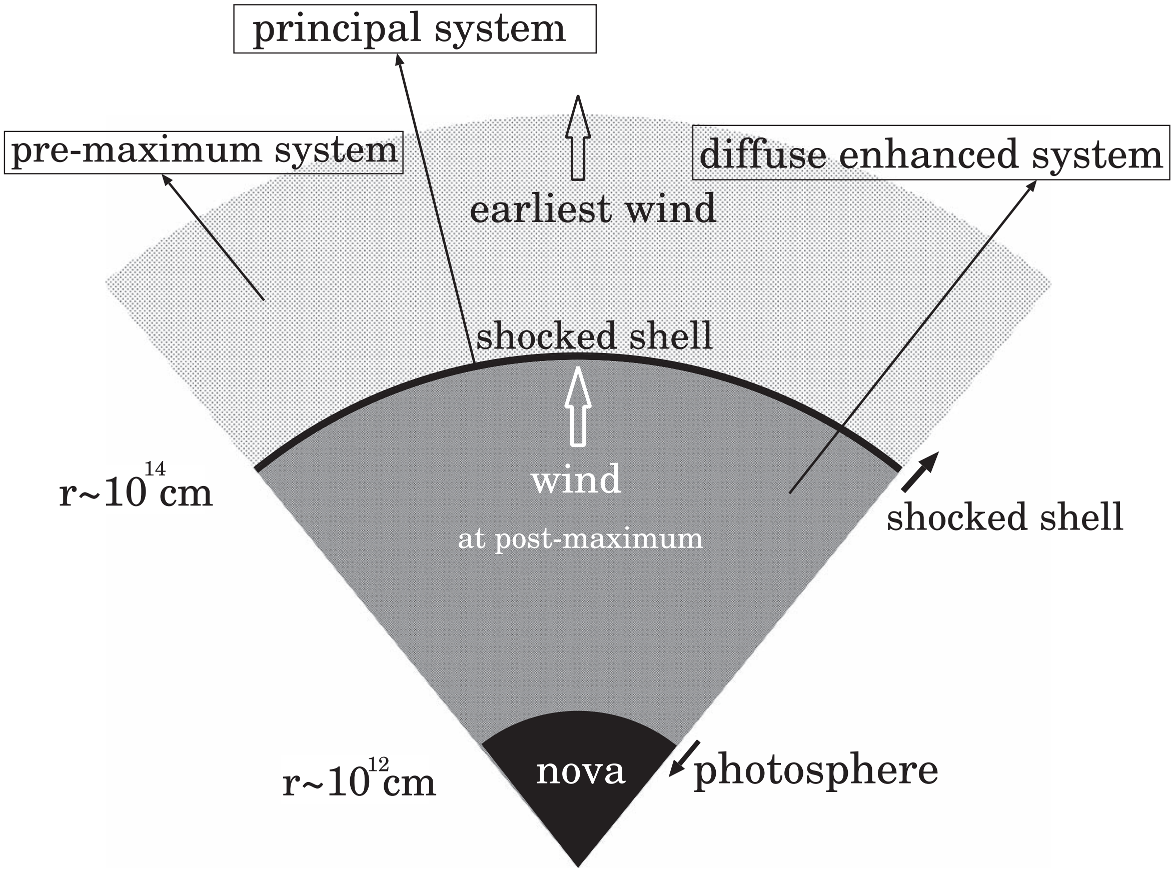

Figure 4. Cartoon of our shocked ejecta model. The shock is formed (at $R_{\rm sh} \sim 10^{13}$–10^{14} cm) far outside the photosphere ($R_{\rm ph} \sim 10^{12}$ cm). The shocked layer is geometrically thin, and the whole ejecta is divided into three parts, outermost expanding gas (earliest wind), shocked thin shell, and inner wind. These three parts contribute to pre-maximum, principal, and diffuse-enhanced absorption/emission line systems (McLaughlin 1942; Mclaughlin 1960), respectively. The shocked shell emits thermal hard X-rays.

Theoretically the shock wave arises outside the photosphere. However, observationally it is called the "internal shock," which simply means that there is a shock in the ejecta.

We calculated the location of the shock, which is shown by the thick red line in Figure 3(a). The location of the shock moves outward and the separation from the photosphere increases with time. Here, we assume that the shocked region cools down in a shorter timescale than a dynamical timescale (isothermal shock; see, e.g., Metzger et al. 2014, 2015; Martin et al. 2018), and the shocked layer is geometrically thin. We can derive the velocity of the shock ($v_{\rm shock}$) from the mass ($M_{\rm shell}$) and momentum ($M_{\rm shell} v_{\rm shock}$) of this thin shell (Chomiuk et al. 2021). The mass of the shocked shell ($M_{\rm shell}$) increases with time and reached about 90% of the total ejecta mass, i.e., $M_{\rm shell} \sim 2.7 \times 10^{-5} M_\odot$. In other words, a large part of nova ejecta is eventually confined to the shocked shell.

2.4. Short Summary

To summarize, we first show a shock generation far outside the nova photosphere, without any arbitrary assumptions on multiple mass ejections. Kato et al. (2022a)'s calculation fully includes thermonuclear runaway, envelope expansion, and wind acceleration in a self-consistent manner. As a result, they obtained temporal change in the wind velocity at the photosphere. The velocity of the wind decreases toward the maximum expansion of the photosphere and turn to increase after that. The wind acceleration is closely related with both the envelope structure and radiative transfer deep inside the photosphere. So, this trend in the temporal change in the wind velocity is common among other nova outbursts even if they have different parameters. Thus, we may conclude that a shock wave generation far outside the photosphere is common among nova outbursts, and it occurs after the maximum expansion of the photosphere. The epoch at the maximum expansion of the photosphere coincides with that of the optical maximum (see Figure 2).

3. Three Velocity Systems

Figure 4 shows a schematic illustration of an expanding nova shell. The shock forms a thin shell, which divides the ejecta into three parts. Correspondingly, we have three velocity components: (1) outermost expanding gas (earliest wind), (2) shocked shell, and (3) wind in the post-maximum phase, i.e., after the maximum expansion of the photosphere (post-maximum wind), as illustrated in Figure 4. These three have velocities of $v_{\rm early} \sim 725$–235 km s^{-1}, $v_{\rm shock} \sim 240$ km s^{-1}, and $v_{\rm wind} \sim 245$–450 km s^{-1}, respectively, at $t \sim 80$ day in Figures 1(a) and 3(a).

The total mass of the shocked shell increases with time, about $M_{\rm shell} \sim 1.2 \times 10^{-5} M_\odot$ at $t = 80$ day, and finally reaches $M_{\rm shell} \sim 2.7 \times 10^{-5} M_\odot$ at $t = 350$ day. The total ejected mass is about $M_{\rm ej} \sim 3.0 \times 10^{-5} M_\odot$ in Kato et al. (2022a)'s model. The other mass of $\Delta M = M_{\rm ej} - M_{\rm shell} \sim 0.3 \times 10^{-5} M_\odot$ forms early expanding matter outside the shocked shell, as shown in Figures 3(a) and 4.

We propose that these three parts of ejecta correspond, respectively, to those that make pre-maximum, principal, and diffuse-enhanced absorption/emission line systems. In the followings we examine these correspondences in more detail.

3.1. Various Features of Principal and Diffuse-enhanced Systems

McLaughlin (1942) pointed out various features of the principal absorption/emission line system in comparison with other velocity systems.

3.1.1. Emergence of Principal System

The principal system becomes dominant a few days after the optical maximum. This property is consistent with our model that a shock emerges after the optical maximum. McLaughlin (1942) also wrote "its displacement is greater than that of the pre-maximum spectrum." The pre-maximum winds have a wide range of velocities, the lowest tail of which is the lowest wind velocity at the optical maximum. So, this can be explained if the velocity of the shocked layer could quickly increase higher than that of the slowest pre-maximum (earlier) winds as can be imagined from Figure 1(a) and Figure 3(a).

3.1.2. Velocities in Principal and Diffuse Enhanced Systems

McLaughlin (1943) listed velocities of pre-maximum, principal, and diffuse-enhanced systems in several novae (in their Tables 3 and 5). These velocities are different from nova to nova, but trends of our three velocity components are qualitatively consistent with the absorption/emission line systems (McLaughlin 1942). For example, the velocities of diffuse-enhanced systems are about double those of principal systems (McLaughlin 1942). In our model, the velocity of the post-maximum wind ($v_{\rm ph} \sim 500$ km s^{-1}) is about double the velocity ($v_{\rm shock} \sim 250$ km s^{-1}) of the shock at $t = 80$ day. This quantitative agreement of the ratio (about double) seems to support our interpretation on the assignment of three parts of ejecta to three absorption/emission line systems.

3.1.3. Dependence on the Nova Speed Class

The velocities of principal absorption systems show a large variation between -300 km s^{-1} and -1500 km s^{-1} (e.g., Table 3 of McLaughlin 1943). Mclaughlin (1960) found an empirical relation between the velocity of principal absorption system $v_{\rm p}$ (km s^{-1}) and the nova speed class t_3 or t_2, i.e.,

$$\log v_{\rm p} = 3.7 - 0.5 \log t_3 = 3.57 - 0.5 \log t_2. \quad (1)$$

Our theoretical nova model produces an optical V light curve as shown in Figure 2, in which we read $t_3 \approx 145$ day (or $t_2 \approx 73$ day). This corresponds to the moderately fast nova class (Payne-Gaposchkin 1957), but close to the slow nova class. Substituting this value into Equation (1), we obtain $v_{\rm p} \approx 400$ km s^{-1} for the principal system of our model. The $v_{\rm shock}$ of our model increases from 240 km s^{-1} at $t = 40$ day to 360 km s^{-1} at $t = 300$ day as seen in Figure 1(a), being broadly consistent with $v_{\rm p} \sim 400$ km s^{-1}.

For the velocity of the diffuse-enhanced absorption system $v_{\rm d}$ (km s^{-1}), Mclaughlin (1960) also obtained an empirical relation of

$$\log v_{\rm d} = 3.81 - 0.4 \log t_3 = 3.71 - 0.4 \log t_2. \quad (2)$$

We have $v_{\rm d} \approx 880$ km s^{-1} for $t_3 \approx 145$ day. The $v_{\rm ph}$ of our model increases from 240 km s^{-1} at $t = 40$ day to 700 km s^{-1} at $t = 300$ day as seen in Figure 1(a). This is a bit small but broadly consistent with $v_{\rm d} \approx 880$ km s^{-1}.

In this way the empirical relations of $v_{\rm p}$–t_3 and $v_{\rm d}$–t_3 are broadly consistent with our model, which suggests our interpretations being reasonable. In what follows, we regard that $v_{\rm p} = v_{\rm shock}$ and $v_{\rm d} = v_{\rm ph}$.

3.2. Origin of Hybrid He/N–Fe II–He/N Novae

Novae are divided into two classes, He/N or Fe II, from their spectral features near the optical maximum (Williams 1992). He/N novae have larger expansion velocities and a higher level of ionization. Fe II type novae evolve more slowly, have a lower level ionization, and show P Cygni components. Williams (1992) regarded that the He/N novae are different from the Fe II novae in the aspect of mass ejection. He wrote "the spectra can be interpreted in terms of a two-component gas consisting of a discrete shell and a continuous wind, in which the narrower Fe II spectrum is formed in the wind, while the broader He/N spectrum is formed in the shell ejected at maximum light." His outer shell/inner wind structure is similar to our shock model in Figure 4, but the velocities of shell and wind are reversed. In our model, the shocked shell has a slower velocity, while the inner winds have much faster velocities.

Tanaka et al. (2011) found that the spectral type of V5558 Sgr evolved from the He/N type toward the Fe II type during a pre-maximum halt and then toward the He/N type again. The recurrent nova T Pyx also shows a similar transition to V5558 Sgr, that is, from He/N to Fe II, and then to He/N again (Izzo et al. 2012; Ederoclite 2014).

In Kato et al. (2022a)'s model, the nova has a high photospheric temperature and tenuous wind (low $\dot{M}_{\rm wind}$) having higher velocities in an early phase as shown in Figure 1(a) ($T_{\rm ph}$ is not shown). The photospheric temperature decreases from 100,000 K to 10,000 K in this early phase (see Figure 2 of Kato et al. (2022a)). These aspects are suitable for a formation of He/N nova.

Then the temperature decreases to $T_{\rm ph} \sim 8000$ K at the optical maximum, which is as low as typical nova temperatures at the optical maximum. The wind mass-loss rate becomes $\dot{M}_{\rm wind} \sim (1\text{–}2) \times 10^{-4}\ M_\odot$ yr^{-1} near the maximum, as massive as the mass-loss rate for typical novae. The mass outflow velocity is also as low as $v_{\rm ph} \sim (200\text{–}300)$ km s^{-1} near the maximum. These properties are consistent with a formation site of narrow line Fe II features (Williams 2012).

In a later phase (post-maximum), the photosphere shrinks and the photospheric temperature increases. The wind mass-loss rate decreases, and its velocity increases. These features are again favorable for a formation of He/N nova. Thus, the evolution of He/N–Fe II–He/N is naturally explained.

3.3. Transient Heavy-element Absorption Features in Novae

Relatively narrow velocity dispersion (∼30–300 km s^{-1}) absorption components were observed in novae near the optical maximum, both before and after the maximum (Williams et al. 2008). Williams et al. (2008) dubbed these narrow absorption line features the Transient Heavy-Element Absorption (THEA) system. They concluded that the THEA gas originates before the outburst and most likely comes from the secondary star. As already mentioned in Section 2.2, our model as well as the three novae, V906 Car, V435 CMa, and V5855 Sgr (see Figure 11 of Aydi et al. 2020a), show slow absorption radial velocities of $\sim$200–250 km s^{-1} near the maximum. These low-velocity components could form THEA features near the maximum, that is, both in the pre-maximum and post-maximum phases because dense winds, $\rho = \dot{M}_{\rm wind}/4\pi r^2 v_{\rm ph}$, as well as the relatively low photospheric temperature of $T_{\rm ph} \sim 8000$ K near the optical maximum (Kato et al. 2022a) are favorable to the formation of the THEA systems.

Aydi et al. (2020a) found that the THEA lines of V906 Car exhibit a slow (pre-maximum) component and an intermediate component, which are essentially identical to the velocities and evolution of the H I, Fe II, O I, and Na I lines, and concluded that the THEA absorptions originate from the same body of gas responsible for the P Cygni profiles in prominent lines. Therefore, we regard that the THEA lines are essentially the same as those of the pre-maximum or principal system proposed by McLaughlin (1942). We further argued that the THEA systems are created by the early/earliest wind (pre-maximum system) or shocked shell (principal system) in Figure 4.

Williams et al. (2008) obtained the excitation temperatures, $T_{\rm exc} \sim 8573$ K (Sc II), 9766 K (Ti II), and 11822 K (Fe II), for the primary THEA system of Nova LMC 2005. They also estimated the mass of THEA system to be as much as $\sim 10^{-5}\,M_\odot$. The excitation temperature is consistent with the photospheric temperature of $T_{\rm ph} \sim$ 8000–10,000 K near the optical maximum in our model (Kato et al. 2022a). The ejecta mass reaches $M_{\rm ej} \sim 0.3 \times 10^{-5}\,M_\odot$ at the optical maximum or increases to $M_{\rm ej} \sim 1.5 \times 10^{-5}\,M_\odot$ at +54 days after the optical maximum in our shock model as already obtained in Section 3. Here, the ejecta mass is calculated to be $M_{\rm ej} = M_{\rm early} + M_{\rm shell} = 0.3 \times 10^{-5}\,M_\odot + 1.2 \times 10^{-5}\,M_\odot = 1.5 \times 10^{-5}\,M_\odot$ at $t = 80$ day (+54 days after the optical maximum), where $M_{\rm early}$ is the total wind mass emitted before the optical maximum. Thus, the mass of the THEA system is also consistent with Williams et al. (2008)'s estimate.

Williams & Mason (2010) wrote "the column density of the absorbing systems, assuming roughly solar abundances, is of the order of $\sim 10^{23}$ cm^{-2} for the THEA systems." Our shocked shell model in Figure 3(c) shows $N_{\rm H} \gtrsim 10^{23}$ cm^{-2} for about 50 days after the optical maximum, which is consistent with Williams & Mason (2010)'s estimate for the THEA systems.

Williams & Mason (2010) also added "since THEA absorption is observed in 80% of novae the gas must exist along most lines of sight, i.e., have a roughly spherical distribution", which is also consistent with our spherically symmetric shocked shell (or pre-maximum wind) model.

Arai et al. (2016) reported the high-dispersion spectroscopic observation (with resolving power of $R \sim 72,\ 000$) of the classical nova V2659 Cyg (Nova Cyg 2014) at 33.05 days after the optical V maximum. Their spectra showed two distinct blueshifted absorption systems originating from H I, Fe II, Ca II, etc. The velocities of the absorption systems are -620 km s^{-1}, and from -1100 to -1500 km s^{-1}, which are dubbed the low-velocity components (LVCs) and high-velocity components (HVCs), respectively. They wrote "the slow radial velocities and the sharp absorption line profiles of the LVCs are consistent with those of THEA reported by Williams et al. (2008) and Williams & Mason (2010)." Thus, we may conclude that the LVCs are essentially the same as those of pre-maximum or principal systems defined by McLaughlin (1942).

Arai et al. (2016) also found that the absorption line profiles of the LVCs show strong asymmetries. Their Figure 5 displays enlarged views of the LVCs of Fe II (42) and Hδ. For all line profiles, the red-side wings of the LVCs are narrower (half-width at half-maximum (HWHM) 30−35 km s^{-1}) than those of the blue-side wing (HWHM 50−70 km s^{-1}). Such a line profile (blueward extension) can be explained in our shock model (see Figures 1(a), 3(a), and 4), because the earliest/earlier winds (before the optical maximum) have larger velocities than the shocked shell, i.e., $v_{\rm early} > v_{\rm shock}$. The main deep absorption is formed by the shocked shell, and the blueward extensions come from the absorption of wind outside the shocked shell (earliest wind in Figure 4).

Tajitsu et al. (2016) reported similar P Cygni absorption profiles of HVCs and LVCs of ^{7}Be II, Fe II (42), and Hγ for V5668 Sgr (at +69 days after the optical maximum) and V2944 Oph (+80 days). The velocities of the absorption systems are -786 km s^{-1} (LVC) and from -1350 to -2200 km s^{-1} (HVCs) for V5668 Sgr (with the resolution of $R \sim 60,\ 000$), -878 km s^{-1} (LVC), and from -1300 to -2000 km s^{-1} (HVCs) for V2944 Oph ($R \sim 45,\ 000$), although the ^{7}Be II $\lambda\lambda$3130.583 and 3131.228 doublet lines coalesce. The LVCs are essentially the same as the THEA systems, which correspond to the principal systems while the HVCs correspond to the diffuse-enhanced systems as mentioned above. ^{7}Be ions have been created during the thermonuclear runaway (TNR) of these novae and decayed to form ^{7}Li within a short period (with a half-life time of 53.22 days). This strongly suggests that the absorbing materials in both HVCs and LVCs consist of products of TNR; that is, the THEA systems are not originated from circumstellar matter ejected before outburst from the companion star as Williams et al. (2008) proposed.

To summarize, the THEA systems are essentially the same as those of LVCs or intermediate-velocity components of Aydi et al. (2020a) and LVCs of Arai et al. (2016) and Tajitsu et al. (2016). These velocity systems are created by the early/earliest wind (pre-maximum systems) or shocked shell (principal systems) near the optical maximum. In our shock model, the asymmetry of LVCs (same as THEA) are naturally explained by absorption of the pre-maximum wind just outside the shocked shell.

4. High-energy Emission from Shocked Matter

A strong shock may also provide high-energy photons. Recently the Fermi Large Area Telescope (Fermi/LAT) detected GeV gamma-ray emissions associated to classical novae (e.g., Abdo et al. 2010; Ackermann et al. 2014; Cheung et al. 2016; Li et al. 2017). These gamma rays are considered to originate from strong shocks (see, e.g., Chomiuk et al. 2021, for a recent review).

To explain GeV gamma-ray emissions from novae, two types of shock formation mechanisms have been proposed. One is the collision between nova ejecta and circumstellar matter (CSM; ejecta–CSM shock model or external shock model) as observed in the symbiotic nova V407 Cyg (e.g., Abdo et al. 2010) and the symbiotic recurrent nova RS Oph (see Cheung et al. 2021a, 2021b; MAGIC Collaboration et al. 2022; H.E.S.S. Collaboration 2022, for the 2021 outburst).

The other type is for novae having a red dwarf (main-sequence star) companion. Such a close binary does not form massive circumstellar matter before a nova outburst. Thus, the hypothesis of "internal shocks" in nova ejecta was proposed to explain hard X-ray emissions (e.g., Friedjung 1987; Lloyd et al. 1992; Mukai & Ishida 2001). These authors assumed multiple shell ejecta that have different velocities. If the inner shell (later ejected) has a larger velocity than that of the outer shell (earlier ejected), the inner one can catch up with the outer one and form a shock wave. This idea is based on the assumption of multiple shell ejections.

In this section, we apply our shock formation model to this idea and examine whether it works or not both for hard X-ray emission and GeV gamma-ray emission.

4.1. Hard X-ray Emission

The temperature just behind the shock is estimated to be

$$kT_{\rm sh} \sim \frac{3}{16}\mu m_p (v_{\rm wind} - v_{\rm shock})^2 \approx 1.0 \text{ keV} \left(\frac{v_{\rm wind} - v_{\rm shock}}{1000 \text{ km s}^{-1}}\right)^2, \tag{3}$$

or

$$T_{\rm sh} \sim 1.1 \times 10^7 \text{ K} \left(\frac{v_{\rm wind} - v_{\rm shock}}{1000 \text{ km s}^{-1}}\right)^2, \tag{4}$$

where k is the Boltzmann constant, $T_{\rm sh}$ is the temperature just after the shock (see, e.g., Metzger et al. 2014), μ is the mean molecular weight ($\mu = 0.5$ for hydrogen plasma), and m_p is the proton mass. Substituting our model values, we obtain the post-shock temperature $kT_{\rm sh}$, as plotted in Figure 3(b) (blue line).

Mechanical energy of wind is converted to thermal energy by the reverse shock at a rate of

$$\begin{aligned} L_{\rm sh} &\sim \frac{9}{32}\dot{M}_{\rm wind}\frac{(v_{\rm wind} - v_{\rm shock})^3}{v_{\rm wind}} \\ &= 1.8 \times 10^{37} \text{ erg s}^{-1}\left(\frac{\dot{M}_{\rm wind}}{10^{-4}\, M_\odot \text{ yr}^{-1}}\right) \\ &\quad \times \left(\frac{v_{\rm wind} - v_{\rm shock}}{1000 \text{ km s}^{-1}}\right)^3 \left(\frac{1000 \text{ km s}^{-1}}{v_{\rm wind}}\right), \end{aligned} \tag{5}$$

which was taken from Metzger et al. (2014). We also plot the time variation of $L_{\rm sh}$ by the red line in Figure 3(b). Both the temperature $kT_{\rm sh}$ and luminosity $L_{\rm sh}$ quickly increase at $t \sim 90$ days after outburst, i.e., about 60 days after the optical peak.

The converted thermal energy, $L_{\rm sh}$, quickly increases to $L_{\rm sh} \sim 10^{35}$ erg s^{-1} in 55 days while the thermal temperature is as low as $kT_{\rm sh} \sim 0.02$ keV at $t \sim 150$ day. This low temperature comes from the small velocity difference, $v_{\rm wind}(t) - v_{\rm shock}(t)$, which is $\sim$140 km s^{-1} in Equations (3) and (4) at $t \sim 150$ day. The wind velocity $v_{\rm wind}(t)$ just in front of the shock is calculated from $v_{\rm wind}(t) = v_{\rm ph}(t - t_{\rm ret})$ and $t_{\rm ret} = (R_{\rm sh}(t) - R_{\rm ph}(t - t_{\rm ret}))/v_{\rm ph}(t - t_{\rm ret})$, where $R_{\rm sh}(t)$ is the present position of shock, $R_{\rm ph}(t - t_{\rm ret})$ and $v_{\rm ph}(t - t_{\rm ret})$ are the photospheric radius and velocity at $t - t_{\rm ret}$, and $t_{\rm ret}$ is the retarded (look back) time, as can be seen in Figure 3(a).

For temperatures of $\sim$0.01–0.05 keV in Figure 3(b), one may expect soft X-ray emissions from thermal plasma in nova ejecta. Such soft X-rays are not observed because the hydrogen column density $N_{\rm H}$ is still as high as $\sim 10^{23}$ cm^{-2} at $t \sim 90$ day as shown in Figure 3(c). Thus, our model for a moderately fast nova predicts no high-energy emissions from the shock because of a small difference in velocities between the wind and shock, i.e., $v_{\rm wind} - v_{\rm shock} \ll 1000$ km s^{-1}.

Hard X-ray emissions are detected in some novae, such as in V838 Her (Lloyd et al. 1992), in V1974 Cyg (Balman et al. 1998), and in V382 Vel (Mukai & Ishida 2001) and interpreted as the shocked ejecta emission.

4.1.1. Velocity Systems in V1974 Cyg

First, we make a qualitative comparison of our model velocities with those in the fast nova V1974 Cyg, of which the three velocity components were well observed, i.e., $v_{\rm early} \sim 5000$ km s^{-1}, $v_{\rm shock} \sim 800$ km s^{-1} (principal spectra), and $v_{\rm wind} \sim 1500$ km s^{-1} (diffuse-enhanced spectra; e.g., Chochol et al. 1997; Cassatella et al. 2004). The velocity of the principal system increases from 800 km s^{-1} (post-maximum) to 1700 km s^{-1} (at $\sim$50 day). Correspondingly, the velocity of the diffuse-enhanced system goes up from 1500 km s^{-1} to 2900 km s^{-1}. This increasing trend is similar to that of our shocked ejecta model.

Chochol et al. (1997) discussed the empirical $v_{\rm p}$–t_3 relation, i.e., $t_3 = 42$ day for V1974 Cyg and $v_{\rm p} \approx 800$ km s^{-1}, which is derived from Equation (1). They discussed that the assignment of $v_{\rm p} \sim 800$ km s^{-1} post-maximum is reasonable as a principal system. More rapidly declining novae have larger velocities of the principal systems.

Simply substituting $v_{\rm wind} - v_{\rm shock} = v_{\rm d} - v_{\rm p} = 1500$–$800 = 700$ km s^{-1} or $= 2900$–$1750 = 1150$ km s^{-1} into Equation (3), we obtain $kT_{\rm sh} \sim 0.5$–1.3 keV, which is broadly consistent with the temperature estimated by Balman et al. (1998). The converted thermal energy generation rate is calculated to be as large as $L_{\rm sh} \sim 1.8 \times 10^{37} \times 1.0 \times (1.15)^3/2.9 \sim 1 \times 10^{37}$ erg s^{-1} for $\dot{M}_{\rm wind} \sim 1 \times 10^{-4}\, M_\odot$ yr^{-1}.

Thus, we can reproduce the temperature of k$T_{\rm sh} \sim 1$–2 keV if we take the observed velocities of $v_{\rm d} - v_{\rm p}$ instead of our model value of $v_{\rm wind} - v_{\rm shock}$. Our original shock formation model based on Kato et al. (2022a)'s calculation has problems in explaining hard X-ray emission of V1974 Cyg.

If we roughly assume that $v_{\rm d} \sim 2 v_{\rm p}$, as summarized by McLaughlin (1942), we have $kT_{\rm sh} \sim 1 \text{ keV}(v_{\rm p}/1000 \text{ km s}^{-1})^2$. We further assume that hard X-ray emission is detected for $kT_{\rm sh} \gtrsim 0.5$ keV. Then, we constrain the nova speed class from Equation (1), that is, $t_3 \lesssim 50$ day, under the condition of $v_{\rm p} \gtrsim 700$ km s^{-1}. The $t_3 \lesssim 50$ day speed class ranges from very fast, fast, and moderately fast novae. We expect the detection of hard X-ray emission from novae to have a speed class of $t_3 \lesssim 50$ day. V838 Her ($t_3 = 4$ day), V1974 Cyg (43 day), and V382 Vel (12 day) all satisfy the $t_3 \lesssim 50$ day speed class (t_3 of these novae are taken from Schaefer 2018).

4.2. GeV Gamma-ray Emission from a Shock

The shock properties that produce GeV gamma-ray emission constrain

$$L_\gamma = \epsilon_{\rm nth}\epsilon_\gamma L_{\rm sh} \sim 10^{35} - 10^{36} \text{ erg s}^{-1}, \tag{6}$$

from observation (Ackermann et al. 2014), where $\epsilon_{\rm nth} \lesssim 0.1$ is the fraction of the shocked thermal energy used to accelerate relativistic nonthermal particles, $\epsilon_\gamma \lesssim 0.1$ the fraction of this energy radiated in the Fermi/LAT band (typically

$\epsilon_{\rm nth}\epsilon_{\gamma} \lesssim 0.03$; Metzger et al. 2015). This simply requires

$$L_{\rm sh} \sim 10^{37} - 10^{38}\ {\rm erg\ s^{-1}}. \tag{7}$$

We may not expect such a large flux of GeV gamma-ray emission from the shocked ejecta in Kato et al. (2022a)'s model because of its small velocity difference, $v_{\rm wind} - v_{\rm shock} \lesssim 300\ {\rm km\ s^{-1}}$ or, in other words, its low shocked luminosity of $L_{\rm sh} \sim 10^{35}\ {\rm erg\ s^{-1}}$ in Figure 3(b).

Here, we examine Fermi acceleration as the source of GeV gamma rays (e.g., Abdo et al. 2010). Li et al. (2017) examined the two processes proposed for gamma rays from novae and preferred proton collisions (hadronic scenario) for V5856 Sgr, rather than inverse Compton/Bremsstrahlung emission (leptonic scenario).

We estimate the timescale of proton–proton (pp) collisions a day after the optical maximum. At radius $R \sim 5 \times 10^{12}$ cm $= 71\, R_{\odot}$, it is about $t_{pp} \approx 1/[4n(R)c\sigma_{pp}] \sim 1000$ s, where c is the speed of light, and $\sigma_{pp} = 3 \times 10^{-26}\ {\rm cm}^2$ is the proton–proton cross section (Abdo et al. 2010). The number density $n(R) \sim 2.6 \times 10^{11}\ {\rm cm}^{-3}$ is calculated from the wind mass-loss rate of our model, $\dot{M}_{\rm wind} = 4\pi r^2 \rho v_{\rm ph} \sim 1.3 \times 10^{-4}\ M_{\odot}\ {\rm yr}^{-1}$.

Eight days later, the shock expands to $R \sim 2.4 \times 10^{13}$ cm. The timescale of proton–proton collision becomes longer but still as short as $t_{pp} \sim 10{,}000$ s $\sim$0.11 day. About a month later, the shock expands to $R \sim 7 \times 10^{13}$ cm $= 1000\, R_{\odot}$, and the timescale becomes $t_{pp} \sim 86,\ 000$ s $\sim$1 day. The collision timescale is short enough for all the protons to interact with each other and to produce π^0 in a day. The temporal variation of $n(R)$ is plotted in Figure 3(c). If we constrain $t_{pp} < 1$ day for gamma-ray detection, its duration is about 35 days. Thus, the shock satisfies the timescale of t_{pp}. However, the shocked energy is too small to explain the GeV gamma-ray fluxes.

Li et al. (2017) estimated the gamma-ray flux from the nova ASASSN-16ma (V5856 Sgr) to be $F_{\gamma} = (4\text{–}8) \times 10^{-10}$ erg cm^{-2} s^{-1}. With the assumed distance to the nova of 4.2 kpc, they obtained the total flux of gamma rays $L_{\gamma} \sim (0.8\text{–}1.6) \times 10^{36}\ {\rm erg\ s^{-1}}$. This corresponds to about a half or fourth of the kinetic energy of wind ($L_{\rm kin} \sim 3 \times 10^{36}\ {\rm erg\ s^{-1}}$) in our model (see Figure 1(b)). Even if all the kinetic energy $L_{\rm kin}$ is converted to the shocked energy $L_{\rm sh}$, the gamma-ray flux L_{γ} is too small to be compatible with the observation because the conversion rate is as small as $L_{\gamma}/L_{\rm sh} \sim 0.03$.

4.2.1. Velocity Systems in V5856 Sgr

For V1974 Cyg in Section 4.1.1 (and V382 Vel in Section 5.4.3), we adopted $v_{\rm p}$ and $v_{\rm d}$ from each author's definition. However, no clear definitions of $v_{\rm p}$ and $v_{\rm d}$ are given in V5856 Sgr.

Aydi et al. (2020a) discussed the relation between old McLaughlin's definition on photographic plates and modern one-dimensional spectra extracted from CCDs. We basically followed their descriptions. Aydi et al. (2020a) wrote "all of the novae show a similar spectral evolution: before the optical peak, the emission lines show P Cygni profiles with absorption troughs at velocities $\sim$200–1000 km s^{-1}. After the optical peak, a broad emission component emerges with the velocities $>$1000 km s^{-1} (more than twice the velocity of the pre-maximum component)." They called the pre-maximum P Cygni profile the slow component and the post-maximum broad emission+higher-velocity P Cygni absorption the fast component. They concluded that these are the same as the pre-maximum and diffuse-enhanced systems of McLaughlin (1944).

Aydi et al. (2020a) also pointed out, on the spectra of V906 Car at the maximum, the coexistence of a new component at a velocity of around 300 km s^{-1} and the slower pre-maximum component at 200 km s^{-1}. They concluded that this intermediate-velocity (300 km s^{-1}) system is what McLaughlin calls the principal system (McLaughlin 1944; Payne-Gaposchkin 1957). They called this the intermediate component.

The slow component is decelerating (slowing down) in the pre-maximum phase, but it appears to be accelerating after the optical maximum (see, e.g., Figure 11 of Aydi et al. 2020a). This trend was interpreted as the replacement of the slow component by the intermediate component (e.g., Aydi et al. 2020a). In our model, the shocked shell (McLaughlin's principal shell), which forms a narrow and deep P Cygni profile, is accelerated by the collision of the fast wind (see also Friedjung 1987). Therefore, the accelerated slow component or intermediate component possibly correspond to the principal system.

Li et al. (2017) reported P Cygni absorption profiles on Hα line of V5856 Sgr, from which we derived the velocity of principal system post-maximum. We measured the velocity at the deepest absorption trough in their Supplementary Figure 2, which is roughly -600 km s^{-1} at -8 day, (=8 day before the optical maximum, discovery date = 2016 October 25 = -14 day), -500 km s^{-1} (-6 day), -800 km s^{-1} (+2 day), -800 km s^{-1} (+4 day). We assign this velocity to $v_{\rm p} = -800$ km s^{-1} post-maximum (+4 day). They also reported that the higher-velocity component appeared and reached 2200 km s^{-1}, so we adopted $v_{\rm d} = 2200$ km s^{-1} post-maximum (+4 day). The velocity difference is $v_{\rm d} - v_{\rm p} = 2200 - 800 = 1400$ km s^{-1} post-maximum (+4 days) of V5856 Sgr.

Then, the shocked thermal temperature is $kT_{\rm sh} = 2.0$ keV from Equation (3), which is high enough to emit hard ($\gtrsim$1 keV) X-rays. The shocked thermal energy generation rate is estimated to be $L_{\rm sh} = 1.8 \times 10^{37} (1.4)^3 / 2.2 \times 1.0 = 2.2 \times 10^{37}\ {\rm erg\ s^{-1}}$ from Equation (5) for $\dot{M}_{\rm wind} = 1.0 \times 10^{-4}\ M_{\odot}\ {\rm yr}^{-1}$. GeV gamma rays were detected from +1 day to +14 day. This shocked thermal luminosity gives a ratio of $L_{\gamma}/L_{\rm sh} \sim 0.04$.

To summarize, in the V5856 Sgr observation, the velocity difference is as large as $v_{\rm wind} - v_{\rm shock} = v_{\rm d} - v_{\rm p} \sim 1400$ km s^{-1} and, as a result, the shock luminosity is large enough to reproduce $L_{\gamma} \sim 0.04 L_{\rm sh} \sim 1 \times 10^{36}\ {\rm erg\ s^{-1}}$ for the wind mass-loss rate of $\dot{M}_{\rm wind} = 1.0 \times 10^{-4}\ M_{\odot}\ {\rm yr}^{-1}$. In what follows, we reproduce the gamma-ray luminosity assuming $v_{\rm shock} = v_{\rm p}$ and $v_{\rm wind} = v_{\rm d}$, which are measured from optical spectra of novae.

5. Discussion

5.1. Super-Eddington Luminosity

A number of nova evolution calculations have been presented, but none of them explained the observed brightnesses of novae that often exceed the Eddington limit (e.g., Della Valle & Izzo 2020). In addition, nova spectra sometimes show a flat pattern, $F_{\nu} \sim$ constant against the frequency ν, different from the blackbody spectrum ([e.g., Gallagher & Ney 1976; Ennis et al. 1977, for one of the brightest novae V1500 Cyg: soon after the optical maximum). Hachisu & Kato (2006) pointed out that free–free emission from nova ejecta outside the photosphere dominates the nova spectra that mainly contribute to the optical luminosity. They proposed a description formula of the free–free flux from nova ejecta as

$$F_\nu \propto \frac{\dot{M}_{\rm wind}^2}{v_{\rm ph}^2 R_{\rm ph}} \tag{8}$$

and define the V-band flux $L_{V,{\rm ff}}$ as

$$L_{V,{\rm ff}} = A_{\rm ff} \frac{\dot{M}_{\rm wind}^2}{v_{\rm ph}^2 R_{\rm ph}}, \tag{9}$$

where the coefficient $A_{\rm ff}$ was determined by Hachisu & Kato (2010, 2015, 2016) and Hachisu et al. (2020). The physical meaning of this formulation is described in more detail in Hachisu et al. (2020). Then, the total V-band flux is

$$L_{V,{\rm total}} = L_{V,{\rm ff}} + L_{V,{\rm ph}}, \tag{10}$$

where $L_{V,{\rm ph}}$ is the V-band flux of $L_{\rm ph}$.

The light curve analysis by Hachisu and Kato, based on the continuous mass loss, reproduces a number of observed multiwavelength light curves of novae, including the super-Eddington phase, which strongly indicates that the current theoretical understanding of mass loss is reasonable (e.g., Hachisu & Kato 2016, 2018b).

We plot the absolute V magnitudes of these fluxes for Kato et al. (2022a)'s model in Figure 2. Here, $m_{V,{\rm total}}$, $m_{V,{\rm ff}}$, and $m_{V,{\rm ph}}$ are the absolute magnitudes obtained from $L_{V,{\rm total}}$, $L_{V,{\rm ff}}$, and $L_{V,{\rm ph}}$, respectively.

It is interesting that three light curves of $m_{V,{\rm total}}$, $m_{V,{\rm ff}}$, and $m_{V,{\rm ph}}$ have a very similar shape. The photospheric V magnitude does not exceed the Eddington limit ($M_V \sim -6$), but the free–free V ($M_V \sim -7.2$) and total V ($M_V \sim -7.5$) magnitudes are much brighter than the Eddington limit ($M_V \sim -6$), where M_V is the absolute V magnitude.

5.2. Enhancement of CNO Elements

Heavy-element enhancement such as C, N, O, and Ne was frequently observed in ejecta of classical novae (e.g., Gehrz et al. 1998). On the other hand, Kato et al. (2022a)'s model does not show heavy-element enrichment because elemental mixing with WD core material does not occur in 1D calculations, and they did not include the additional dredging-up mechanism. In this subsection, we examine how such heavy-element enhancement alters shock wave and gamma-ray emission.

Here we use the steady-state wind model calculated by Kato & Hachisu (1994) because no fully self-consistent models are presented for the case of heavy-element enrichment. This steady-state model is a good approximation of the decay phase of a nova outburst (Kato et al. 2022a).

Figure 5 shows optical V light curves of novae (free–free emission) but for a CNO enhancement model, $X = 0.45$, $Y = 0.18$, $Z = 0.02$, $X_{\rm C} = 0.15$, and $X_{\rm O} = 0.20$ by mass weight (see Hachisu & Kato 2006, 2010, 2016, 2017, for detail). They dubbed this chemical composition model "CO nova 3 (CO3)." For comparison, we choose the 0.98 $M_\odot$ WD model, which corresponds to a typical fast nova and reproduces the multiwavelength light curves of V1668 Cyg (e.g., Hachisu & Kato 2016) as shown in Figure 6(a). The temporal variations of photospheric values in Figures 7 and 8 are essentially similar to those in Figures 1 and 3, respectively. We plot physical values after the optical maximum, because a shock is generated only after the optical maximum, and a steady state is established after the optical maximum (Kato et al. 2022a).

The largest difference is the duration of the wind phase, about 3 times shorter, in the 0.98 $M_\odot$ (CO3) model than in our model in Section 2. The photospheric velocity is about $\sim$200 km s^{-1} ($\sim$30%) faster. The wind mass-loss rate is slightly larger. These differences mainly come from (i) less fuel of hydrogen ($X = 0.65$ versus $X = 0.45$), (ii) smaller ignition mass in heavy-element enrichment models (e.g., Chen et al. 2019), and (iii) larger acceleration owing to the radiation-pressure gradient. We have already discussed these differences in more detail in Kato et al. (2022a).

The velocity difference is still as low as $v_{\rm wind} - v_{\rm shock} = v_{\rm ph}(t - t_{\rm ret}) - v_{\rm sh}(t) \approx 452–311 = 141$ km s^{-1} at $t = 40$ day as can be seen in Figures 7(a) and 8(a), so that the temperature is as low as $kT_{\rm sh} \sim 0.02$ keV, essentially the same as in Figure 3(b). We expect soft X-ray emission from the shocked matter. Such soft X-rays are not observable due to heavy absorption ($\log N_{\rm H} \sim 23–24$) as shown in Figure 8(c).

As for GeV gamma-ray emission, the shocked thermal energy generation rate is as small as $L_{\rm sh} \lesssim 0.01 \times 10^{36}$ erg s^{-1} post-maximum (Figure 8(b)), much smaller than $L_\gamma \sim (0.8–1.6) \times 10^{36}$ erg s^{-1} (for V5856 Sgr; Li et al. 2017). Even if we use a CNO-enriched model of 0.98 $M_\odot$ WD, we cannot reproduce the early GeV gamma-ray emission like in V5856 Sgr.

5.3. V1974 Cyg 1992

5.3.1. Model Light Curve Fitting of V1974 Cyg

Figure 6(b) shows the absolute magnitudes of V light curves for each component, i.e., the photospheric (red line, labeled BB), free–free emission (blue, FF), and the total of them (green, TOTAL). This model light curve (green line) reproduces well the observed V light curve (filled blue circles) of V1974 Cyg if we adopt the V-band distance modulus, $(m - M)_V = A_V + 5\log(d/10~{\rm pc}) = 0.93 + 5\log(1.6~{\rm kpc}/10~{\rm pc}) = 12.0$, where, the V-band absorption of $A_V = 0.93$ is taken from Hachisu & Kato (2019a) and Hachisu & Kato (2021) and the distance of $d = 1.6$ kpc is from Gaia early data release 3 (EDR3; Bailer-Jones et al. 2021).

Because the V-band distance modulus is fixed to $(m - M)_V = 12.0$, we have only one degree of freedom, that is, shifting the model light curves back and forth horizontally. In the figure, we fit our total V model light curves with the optical maximum. The model light curve labeled TOTAL reasonably follows the V data of V1974 Cyg in an early phase (up to $\sim$90 days after the optical maximum). After that, the model light curve deviates downward largely from the visual and V data. This is because strong emission lines such as [O III] significantly contribute to the V-band flux as discussed by Hachisu & Kato (2006). If we could use the intermediate y-band magnitude, which avoids strong emission lines such as [O III], our model light curve follows well the continuum flux of the nova even in the nebular phase, as seen in Figure 6(a) of V1668 Cyg. Thus, the continuum flux of the nova decreases almost along with the model light curve. Therefore, we adopt the 0.98 $M_\odot$ as a good model both for V1668 Cyg and V1974 Cyg.

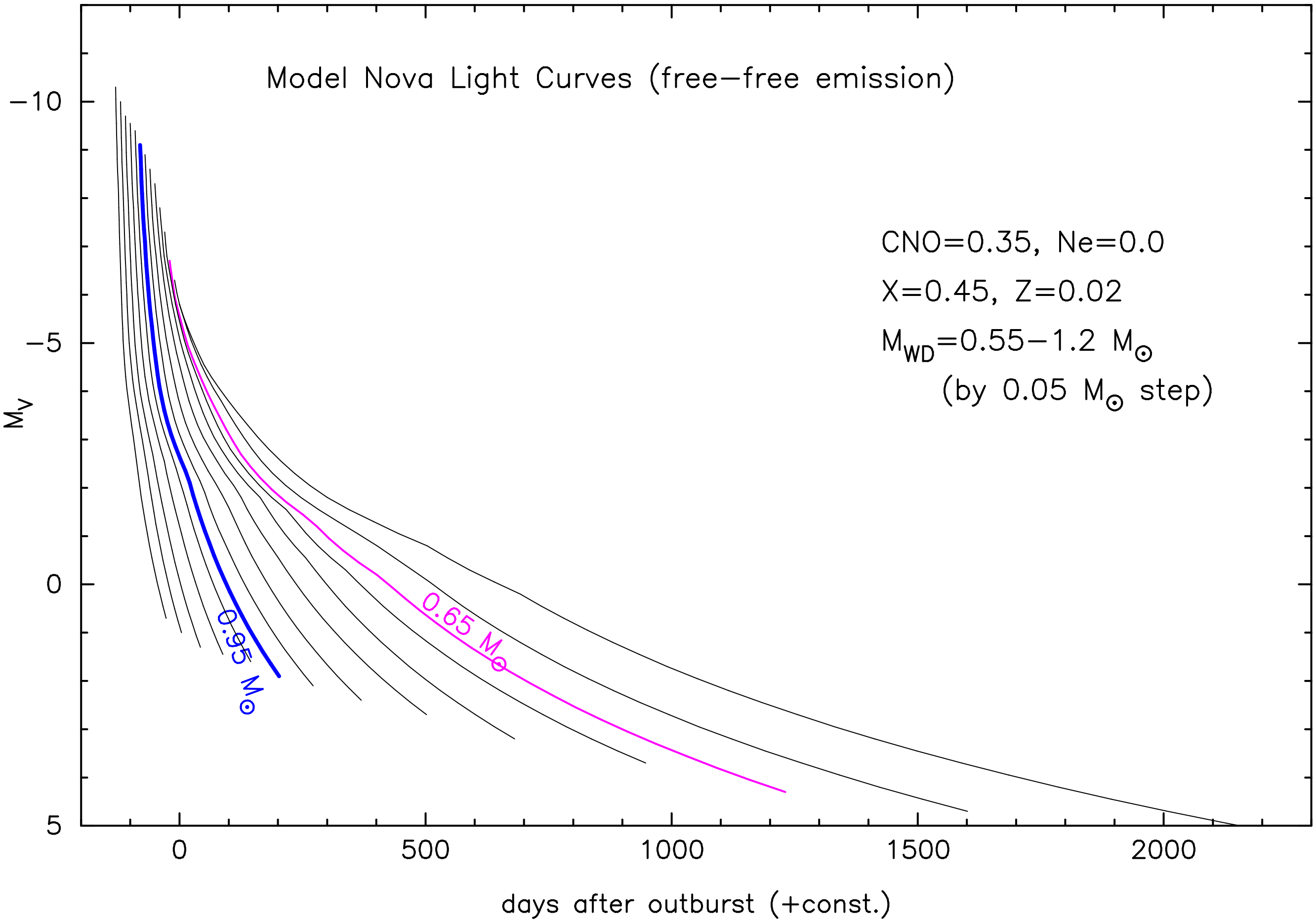

Figure 5. Absolute V light curves of free–free emission for various WD masses, i.e., $M_{\rm WD} = 0.55$, 0.6, 0.65, 0.7, 0.75, 0.8, 0.85, 0.9, 0.95, 1.0, 1.05, 1.1, 1.15, and 1.2 $M_\odot$ with the chemical composition of the hydrogen-rich envelope of $X = 0.45$, $Y = 0.18$, $Z = 0.02$, $X_{\rm C} = 0.15$, and $X_{\rm O} = 0.20$ (see Hachisu & Kato 2006, 2016). Hachisu & Kato (2006) called this chemical composition "CO nova 3 (CO3)". The proportionality constant $A_{\rm ff}$ in Equation (9) was calibrated by Hachisu & Kato (2016) and Hachisu et al. (2020). Various nova parameters are calculated from the steady-state envelope solutions given by Kato & Hachisu (1994). The 0.95 $M_\odot$ model (blue line) corresponds to typical fast novae while the 0.65 $M_\odot$ model (magenta line) is a representative for slow or very slow novae.

We should note that V1974 Cyg was identified as a neon nova (e.g., Shore et al. 1997; Vanlandingham et al. 2005, for the neon abundance). In Figure 6(b), we used a CNO-rich composition (from our template models in Figure 5) instead of a neon-rich composition because the enrichment of neon with unchanged hydrogen and CNO mass fractions affects the nova light curves very little in our model light curves. This can be justified by the result that neon is not relevant to either nuclear burning (the CNO cycle) or the opacity (see Hachisu & Kato 2016, for more detail).

5.3.2. Absorption/emission Line Systems in V1974 Cyg

Our 0.98 $M_\odot$ WD model reasonably reproduced the V (as well as UV 1455 Å and soft X-ray) light curve (see Hachisu & Kato 2016, for more details). However, the velocities of absorption/emission line systems are largely different from the observation. We summarize the model versus observation as follows. Principal system: 240 versus 800 km s^{-1} just post-maximum, 400 versus 1750 km s^{-1} at ∼60 days after maximum. Diffuse-enhanced system: 240 versus 1500 km s^{-1} just post-maximum, 580 versus 2900 km s^{-1} at ∼60 days after maximum. The observed velocities, which are taken from Chochol et al. (1997) and Cassatella et al. (2004), are 4 times larger than those in our model.

If our interpretation of $v_{\rm shock} = v_{\rm p}$ and $v_{\rm wind} = v_{\rm d}$ is correct, our steady-state wind model lacks some additional acceleration mechanisms inside or outside the photosphere.[4] In what follows, we adopt $v_{\rm shock} = v_{\rm p}$ and $v_{\rm wind} = v_{\rm d}$ and discuss the energy and temperature of high-energy emissions.

5.3.3. Hard X-Ray Emission in V1974 Cyg

As already discussed in Section 4.1, we obtain sufficiently high shocked temperatures of $kT_{\rm sh} \sim$ 1–2 keV, which is consistent with Balman et al. (1998)'s estimate, if we use the observed principal ($v_{\rm p}$) and diffuse-enhanced ($v_{\rm d}$) velocities in V1974 Cyg. Then, the thermal energy generation rate is as large as $L_{\rm sh} \sim 1.5 \times 10^{37}$ erg s^{-1} just post-maximum for the wind mass-loss rate of $\dot{M}_{\rm wind} = 1.6 \times 10^{-4}\, M_\odot$ yr^{-1}. It decreases to $L_{\rm sh} \sim 2.0 \times 10^{36}$ erg s^{-1} 60 days after the maximum for the wind mass-loss rate of $\dot{M}_{\rm wind} = 0.12 \times 10^{-4}\, M_\odot$ yr^{-1}, which is large enough to explain the hard X-ray flux of $L_{\rm hx} \sim (0.8\text{–}2) \times 10^{34}$ erg s^{-1} estimated by Balman et al. (1998). The conversion rate to X-rays in our model is as small as $L_X/L_{\rm sh} \sim 0.01$ at day +60.

The column density of hydrogen is estimated from $M_{\rm shell} = 4\pi R_{\rm sh}^2 \rho h_{\rm shell}$, where ρ is the density in the shocked

---

[4] Note that the revised opacity tables (OPAL or OP in the 1990s) drastically changed nova calculations, and the obtained expansion velocities are multiplied.

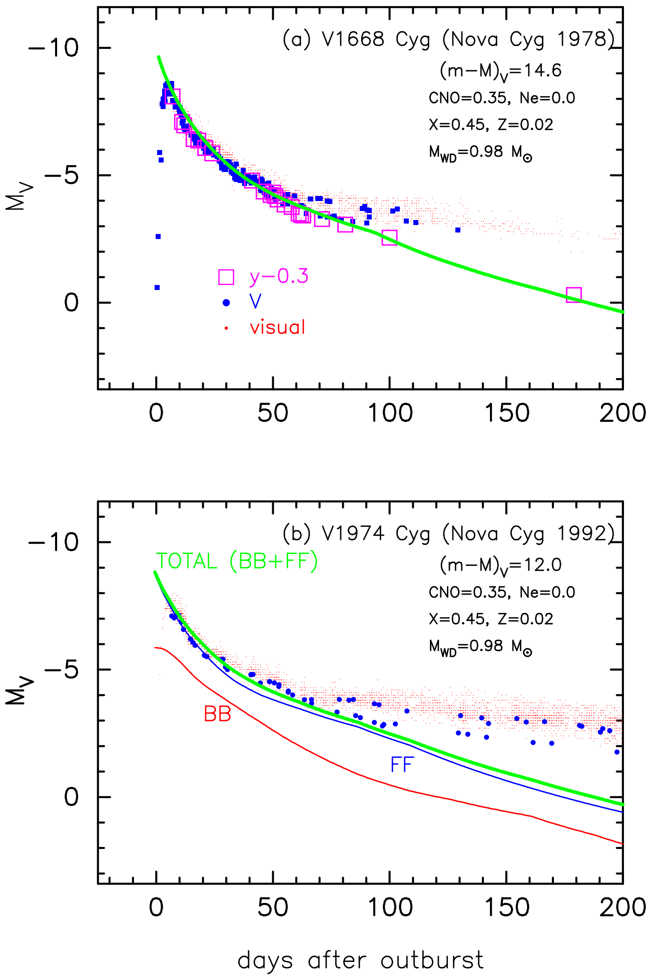

Figure 6. Same as those in Figure 2, but for a 0.98 $M_\odot$ WD with CNO enhancement (CO3). Only the decay phase (after the optical maximum) of the steady-state model in Figure 5 (Kato & Hachisu 1994; Hachisu & Kato 2006) is plotted. The solid red line denotes blackbody emission from the photosphere (labeled BB). The solid blue line is free–free emission (labeled FF). The thick solid green lines are the total flux (labeled TOTAL) of BB and FF. (a) The 0.98 $M_\odot$ WD model light curve is fitted with the visual (red dots), V (filled blue circles), and y (open magenta squares) light curves of V1668 Cyg. The visual magnitudes are taken from the archive of the American Association of Variable Star Observers (AAVSO), and those of V magnitudes are from di Paolantonio et al. (1981), Piccioni et al. (1984), Hopp (1979), Kolotilov (1980), Mallama & Skillman (1979), and Duerbeck et al. (1980). The data of the y magnitudes are from Gallagher et al. (1980). (b) Same as panel (a) but for V1974 Cyg. The visual data are taken from AAVSO; the V data are taken from Chochol et al. (1993).

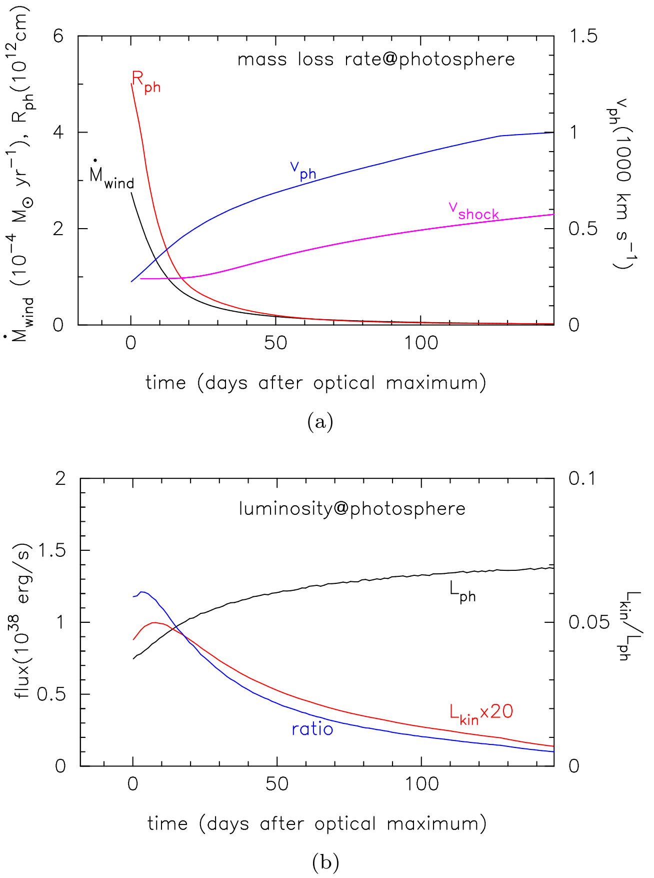

(a)

(b)

Figure 7. Same as those in Figure 1, but for a 0.98 $M_\odot$ WD with CNO enhancement (CO3). The time $t = 0$ correspond to the optical maximum. Only the decay phase (after the optical maximum) of steady-state envelope model is plotted.

shell, and $h_{\rm shell}$ the thickness of the shocked shell. If we take an averaged velocity of shell $v_{\rm sh} = v_{\rm shell} = v_{\rm shock}$, the shock radius is calculated from $R_{\rm sh}(t) = v_{\rm shock} \times t$. This reads

$$\begin{aligned} N_{\rm H} &= \frac{X}{m_p}\frac{M_{\rm shell}}{4\pi R_{\rm sh}^2} \\ &\approx 4.8\times 10^{22}\ {\rm cm}^{-2}\left(\frac{X}{0.5}\right)\left(\frac{M_{\rm shell}}{10^{-5}M_\odot}\right)\left(\frac{R_{\rm sh}}{10^{14}\ {\rm cm}}\right)^{-2} \\ &\approx 6.4\times 10^{20}\ {\rm cm}^{-2}\left(\frac{X}{0.5}\right)\left(\frac{M_{\rm shell}}{10^{-5}M_\odot}\right) \\ &\quad\times\left(\frac{v_{\rm shell}}{1000\ {\rm km\ s}^{-1}}\right)^{-2}\left(\frac{t}{100\ {\rm day}}\right)^{-2}. \end{aligned} \tag{11}$$

We assume that, when the column density becomes as low as $N_{\rm H} \sim 10^{21}$ cm^{-2}, hard X-rays (1–10 keV) can diffuse out from the shocked shell. Then, we have the emergence time of

$$\begin{aligned} t \approx 80\ {\rm day}&\left(\frac{X}{0.5}\right)^{-\frac{1}{2}}\left(\frac{M_{\rm shell}}{10^{-5}M_\odot}\right)^{\frac{1}{2}} \\ &\times\left(\frac{N_{\rm H}}{10^{21}\ {\rm cm}^{-2}}\right)^{-\frac{1}{2}}\left(\frac{v_{\rm shock}}{1000\ {\rm km\ s}^{-1}}\right)^{-1}. \end{aligned} \tag{12}$$

We obtain the ejecta mass of $M_{\rm ej} = 0.95 \times 10^{-5}\,M_\odot$ from the light curve fitting in Figure 6(b). The average shock velocity is $v_{\rm shock} = v_{\rm p} = (800 + 1750)/2 \sim 1300$ km s^{-1} from the principal absorption system in V1974 Cyg (Chochol et al. 1997). Substituting these two values into Equation (12), we have $t \sim 63$ day for $N_{\rm H} \sim 10^{21}$ cm^{-2}. This is consistent with the hard X-ray emergence time $t \sim 60$ day of V1974 Cyg obtained by Balman et al. (1998).

Just post-maximum ($t \sim 1$ day), we obtain $M_{\rm shell} \approx 0.05 \times 10^{-5}\,M_\odot$ and $R_{\rm sh} \sim 1 \times 10^{13}$ cm from the fitted model. Then, this gives $N_{\rm H} = 2 \times 10^{23}$ cm^{-2} for $X = 0.45$. Therefore, we could not detect hard X-ray emission near the optical maximum due to absorption by hydrogen behind the shock.

The optical depth for X-ray is estimated to be

$$\begin{aligned} \tau_X \approx 8\times 10^{3}&\left(\frac{\dot M_{\rm wind}}{10^{-4}M_\odot\ {\rm yr}^{-1}}\right)\left(\frac{r}{10^{13}\ {\rm cm}}\right)^{-1} \\ &\times\left(\frac{v_{\rm wind}}{400\ {\rm km\ s}^{-1}}\right)^{-1}\left(\frac{E_X}{\rm keV}\right)^{-2}, \end{aligned} \tag{13}$$

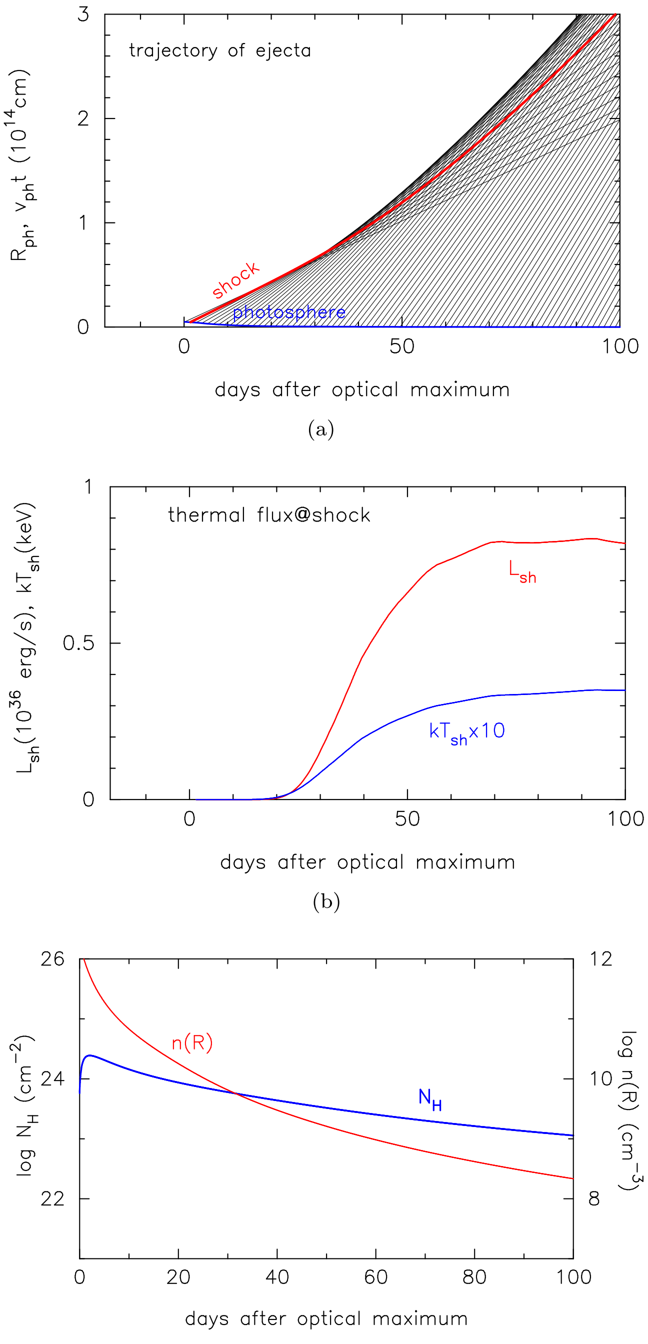

(a)

(b)

(c)

Figure 8. Same as in Figure 3, but for a 0.98 $M_\odot$ WD with CNO enhancement (CO3). Only the decay phase (after the optical maximum) of steady-state envelope model is plotted. (a) A strong shock forms soon after the optical maximum and expands outward at a speed of 250–600 km s^{-1}. (b) Both the shocked luminosity L_{sh} (red) and temperature kT_{sh} (blue) quickly rise up ∼30 days after the optical maximum. (c) Temporal changes in the column density N_H and number density $n(R)$, slightly denser than those of the 1.0 $M_\odot$ model in Figure 3(c).

which is taken from Equation (9) of Li et al. (2017). The optical depth is as high as $\tau_X \sim 10^3 (E_X/\text{keV})^{-2}$ post-maximum, but it decreases to $\tau_X \sim 10 (E_X/\text{keV})^{-2}$ at ∼60 days after maximum. Thus, hard X-ray emission could be observable at ∼60 days after the maximum and later.

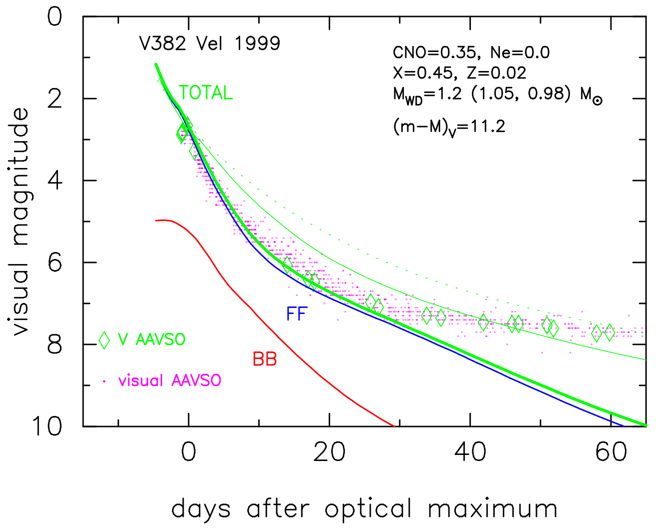

Figure 9. Optical visual (magenta dots) and V (open green diamonds) magnitudes of the classical nova V382 Vel are plotted on a linear timescale. The visual and V data are taken from AAVSO. We assume the V-band distance modulus of $(m-M)_V = 11.2$ to the nova, i.e., $A_V + 5\log(d/10\ \text{pc}) = 0.3 + 5\log(1.5\ \text{kpc}/10\ \text{pc}) = 11.2$. We plot our best-fit model of 1.2 $M_\odot$ WD, that is, the red line denotes the blackbody emission from the photosphere (labeled BB), the blue line is the free–free emission light curve (labeled FF), and the green line corresponds to the total flux of FF and BB (labeled TOTAL). Only the decay phase of the steady-state envelope model is plotted. We also plot the total emission (BB+FF) model light curves for another two WD mass models, 1.05 $M_\odot$ (thin solid green line) and 0.98 $M_\odot$ (thin dotted green line). We select the 1.2 $M_\odot$ model as the best-fit model among the three mass models with the chemical composition of CO3.

5.4. V382 Vel 1999

5.4.1. Model Light Curve Fitting of V382 Vel

Figure 9 shows our model light curve fitting (see, e.g., Hachisu & Kato 2019b, for more details). We adopt a 1.2 $M_\odot$ WD model as the best-fit one among the three, 0.98, 1.05, and 1.2 $M_\odot$. Here, we assume a V-band distance modulus of $(m-M)_V = A_V + 5\log(d/10\ \text{pc}) = 0.3 + 5\log(1.5\ \text{kpc}/10\ \text{pc}) = 11.2$, where a relatively low extinction $A_V \approx 0.3$ is taken from Della Valle et al. (2002), and the distance is taken from Gaia EDR3 (Bailer-Jones et al.2021).

The V-band distance modulus is fixed to $(m-M)_V = 11.2$, so that we have only one degree of freedom, that is, shifting the model light curves back and forth horizontally. In the figure, we fit our three (total V) model light curves with the optical maximum. The model light curve labeled TOTAL reasonably follows the visual and V data of V382 Vel in an early phase (up to ∼30 days after the optical maximum). After that, the model light curve deviates downward largely from the visual and V data. This is because strong emission lines such as [O III] significantly contribute to the V-band flux as already discussed in Section 5.3.1. Thus, the continuum flux of the nova decreases almost along with the model light curve. Therefore, we adopt the 1.2 $M_\odot$ as the best-fit one among the three model light curves.

The optically thick wind of this 1.2 $M_\odot$ WD model ends at $t \sim 95$ days after the optical maximum. The hydrogen shell burning stops at $t \sim 190$ days after the optical maximum. These features are broadly consistent with the decay of supersoft X-ray phase observed with BeppoSAX (Orio et al. 2002). See Hachisu & Kato (2016) for more details.

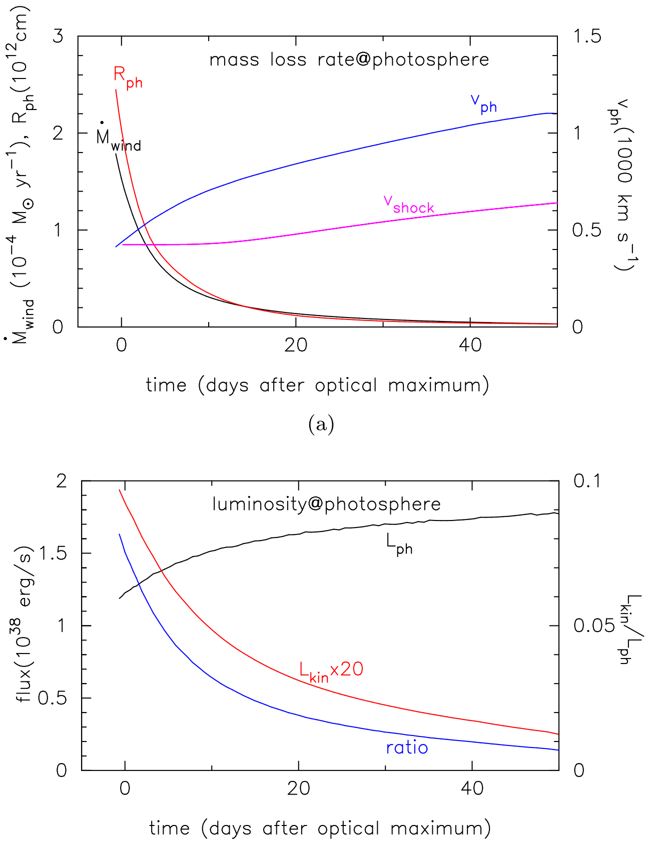

(a)

(b)

Figure 10. Same as those in Figure 1, but for a 1.2 $M_\odot$ WD with CNO enhancement (CO3). Only the decay phase (after the optical maximum) of steady-state envelope model is plotted. The time $t = 0$ corresponds to the optical maximum.

5.4.2. Shock Formation Outside the Photosphere

Figures 10 and 11 show the same physical quantities as in Figures 1 and 3, respectively, but for a 1.2 $M_\odot$ (CO3) model. A strong shock arises outside the photosphere and expands at a velocity of $v_{sh}(=v_{shock}) \approx 400$–$700\ \mathrm{km\ s^{-1}}$, as shown in Figures 10(a) and 11(a). The main differences from the 0.98 $M_\odot$ model are (i) the wind velocity is faster in the 1.2 $M_\odot$, 400 (versus 250) km s^{-1} soon after the optical maximum, and 1100 (versus 1000) km s^{-1} in a later phase; as a result, (ii) the shock velocity is faster in the 1.2 $M_\odot$, 400 (versus 250) km s^{-1} soon after the optical maximum, but similar to 700 (versus 600) km s^{-1} in a later phase; (iii) the duration of wind phase is much shorter in the 1.2 $M_\odot$, 95 days (versus 250 days). Thus, the evolution timescale is about 2.5 times shorter in the 1.2 $M_\odot$ model.

5.4.3. Velocity Systems in V382 Vel

The temperature just behind the shock is obtained to be $\sim$0.03 keV as shown in Figure 11(b). This temperature is much smaller than those estimated from hard X-ray emission by Mukai & Ishida (2001). The velocities of the principal and diffuse-enhanced systems in V382 Vel were obtained by Della Valle et al. (2002) to be $v_p \sim 2300\ \mathrm{km\ s^{-1}}$ and $v_d \sim 3700\ \mathrm{km\ s^{-1}}$ post-maximum. Our $v_{shock} = v_p \sim 400\ \mathrm{km\ s^{-1}}$ is about 6 times smaller than that of V382 Vel. Simply substituting the observed values $v_{wind} - v_{shock} = v_d - v_p = 3700 - 2300 = 1400\ \mathrm{km\ s^{-1}}$, we obtain $kT_{sh} \sim 2$ keV, which is consistent with the temperature estimated by Mukai & Ishida (2001).

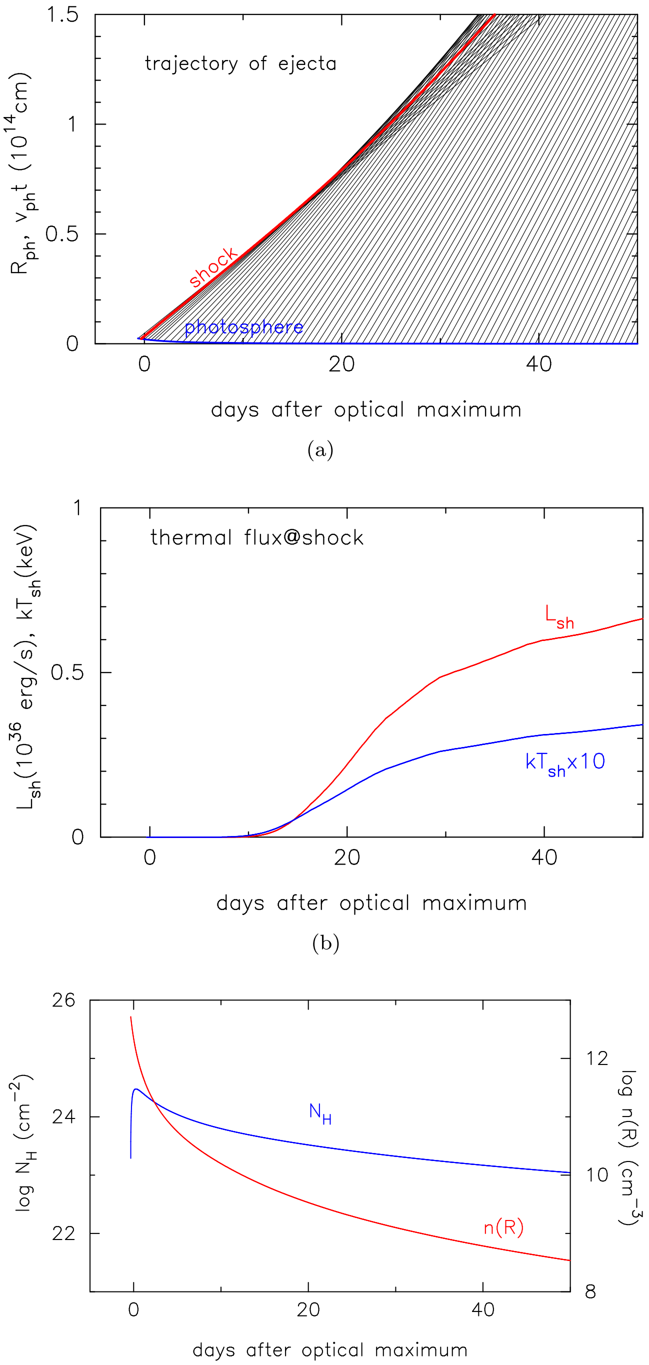

(a)

(b)

(c)

Figure 11. Same as in Figure 3, but for a 1.2 $M_\odot$ WD with CNO enhancement (CO3). Only the decay phase (after the optical maximum) of the steady-state envelope model is plotted. (a) A strong shock arises soon after the optical maximum and expands outward at a speed of 400–700 km s^{-1}. (b) Both the shocked luminosity L_{sh} (red) and temperature kT_{sh} (blue) quickly rise up $\sim$15 days after the optical maximum. (c) The N_H is still as high as a few times $10^{23}\ \mathrm{cm^{-2}}$ at $t \sim 20$ days after the optical maximum.

5.4.4. Hard X-Ray Emission from V382 Vel

Hard X-ray emission from V382 Vel was detected with ASCA and RXTE from about 20 days to 60 days past the optical peak (Mukai & Ishida 2001). The column density of hydrogen is estimated from Equation (11) together with $v_{shock} = v_p = 2300\ \mathrm{km\ s^{-1}}$. We obtain the ejecta mass of $M_{ej} \sim 0.51 \times 10^{-5}\ M_\odot$ from the light curve fitting in Figure 9.

Substituting these values into Equation (11), we have $N_{\rm H} = 1.3 \times 10^{21}$ cm^{-1} at $t \sim 20$ day and $N_{\rm H} = 2 \times 10^{20}$ cm^{-1} at $t \sim 50$ day, both of which are low enough for X-ray photons to diffuse out from the shell.

The thermal energy generation rate is as large as $L_{\rm sh} \sim 1.8 \times 10^{37} \times (1.4)^3/3.7 = 2.6 \times 10^{37}$ erg s^{-1} from Equation (5) for $\dot{M}_{\rm wind} = 2 \times 10^{-4} M_\odot$ yr^{-1} near post-maximum, which decreases to $L_{\rm sh} \sim 2.7 \times 10^{36}$ erg s^{-1} for $\dot{M}_{\rm wind} = 2 \times 10^{-5} M_\odot$ yr^{-1} at $\sim$50 day after the maximum. Here, with the relation of $t_{\rm ret} = t \times (v_{\rm p}/v_{\rm d})$, we have $t_{\rm ret} \sim t \times (2300/3700) = 0.62t$, that is, $t_{\rm ret} = 50 \times 0.62 = 31$ day. If we take the retarded (look back) time $t_{\rm ret}$ into account, the wind mass-loss rate measured at the photosphere decreases to $\dot{M}_{\rm wind} = 2.0 \times 10^{-5} M_\odot$ yr^{-1} in our 1.2 $M_\odot$ WD (CO3) model at +19 day. The shock luminosity $L_{\rm sh} \sim 2.7 \times 10^{36}$ erg s^{-1} is sufficiently larger than $L_X \sim 7 \times 10^{34}$ erg s^{-1}, estimated by Mukai & Ishida (2001) at $\sim$50 day after maximum. Then the conversion rate to X-ray emission is rather small, i.e., $L_X/L_{\rm sh} \sim 0.026$.

Thus, our shock model of a nova reasonably explains the hard X-ray emission from V382 Vel.

5.5. ASASSN-16ma (V5856 Sgr 2016)

Li et al. (2017) reported the Fermi/LAT observation of the classical nova ASASSN-16ma (a.k.a. V5856 Sgr). Its dense observation provides high-quality information. We summarize their results and implications as follows.

1. The first gamma-ray emission is detected shortly after the optical maximum. They have no positive detection before the optical maximum.
2. The gamma-ray flux decays to almost follow the decline trend of the optical flux. The ratio of the gamma-ray flux to the optical flux is almost constant, $L_\gamma/L_{\rm opt} \sim 0.002$.
3. From a remarkable correlation between the gamma-ray and optical fluxes, they concluded that the majority of the optical light comes from reprocessed emission from shocks rather than the WD.
4. Their assumed model is such that: after the thermonuclear runaway, the WD loses its mass by slow winds that escape from the binary through the outer Lagrangian (L2) point to form circumbinary matter. Then, the wind becomes faster and collides with the circumbinary matter.
5. A strong shock arises deep inside the circumbinary matter, where gas is optically thick for X-rays so that all the X-ray photons are reprocessed to lower-wavelength photons (UV and optical). GeV gamma rays diffuse out from the shocked layer because its optical depth is small.

A similar property to their point 1 was reported in two classical novae with a short orbital period, V339 Del ($P_{\rm orb} = 3.154$ hr in Chochol et al. 2015) and V1324 Sco ($P_{\rm orb} = 3.8$ hr in Finzell et al. 2018); the Fermi/LAT > 100 MeV flux peaked a few to several days after the optical maximum (see Figure 3 of Cheung et al. 2015).

For their point 2, no clear correlation is seen in the V549 Vel outburst (Li et al. 2020) and YZ Ret outburst (König et al. 2022; Sokolovsky et al. 2022). So it may not be common among all the gamma-ray novae.

The time sequence of the GeV gamma-ray and optical light curves are as follows:

1. The nova optically brightens up to $m_V \sim 8$ over two weeks, and there is no detection of GeV gamma rays during this rising phase (Phase I).
2. Then its brightness rapidly increased by a factor of 10 in two days, reaching an optical maximum of $m_V \sim 5.4$ (Phase II). GeV gamma rays were detected soon after this optical maximum.
3. The gamma-ray flux declined with being well correlated to the decay of the optical flux until 9 days after the optical maximum (Phase III). They concluded that the duration of detectable gamma-ray emission is 9–15 days.
4. No hard X-rays (1–10 keV) were detected by Swift/XRT around the optical maximum or five months later.

The optical and gamma-ray light curves are plotted in Figure 12(a). We discuss GeV gamma-ray fluxes from V5856 Sgr, assuming that $v_{\rm shock} = v_{\rm p}$ and $v_{\rm wind} = v_{\rm d}$.

5.5.1. Model Light Curve Fitting

Figure 12(a) shows our model light curve fitting. We adopt a 1.3 $M_\odot$ WD model as the best-fit one among the three, 1.3, 1.2, and 1.1 $M_\odot$, but for the envelope chemical composition of neon nova 2 (Ne2), i.e., $X = 0.55$, $Y = 0.30$, $Z = 0.02$, $X_{\rm O} = 0.10$, and $X_{\rm Ne} = 0.03$ (e.g., Kato & Hachisu 1994; Hachisu & Kato 2006, 2010). This is because such a heavy WD is composed of an oxygen/neon core (e.g., Umeda et al. 1999). Here, we assume a V-band distance modulus of $(m - M)_V = A_V + 5 \log(d/10 \text{ pc}) = 14.4$. This value is an arithmetic mean between those of Li et al. (2017) and Munari et al. (2017).

Because the V-band distance modulus is fixed to $(m - M)_V = 14.4$, we have only one degree of freedom, that is, shifting the model light curves back and forth horizontally. In the figure, we fit our three (total V) model light curves with the optical maximum. Although the midway data points are slightly above the model line, the late data around 40 days after the optical maximum are just on the model line (thick green line). Therefore, we adopt the 1.3 $M_\odot$ as the best-fit one.

We also plot the gamma-ray fluxes (open magenta diamonds) in the figure. Qualitatively, the trend of the gamma-ray decay follows well the trend of the optical V decay. In our model, the flux of free–free emission dominates and is given by $L_{V,\rm ff} \propto (\dot{M}_{\rm wind}/v_{\rm ph})^2$ while the flux of the gamma rays is given by $L_{\gamma,\rm sh} \propto (\dot{M}_{\rm wind}/v_{\rm wind})$. Thus, the dependency on $(\dot{M}/v)^n$ is similar, but the power of n is different by a factor of 2 ($n = 2$ versus $n = 1$). Therefore, the light curves in magnitudes are written as

$$\begin{aligned} \frac{1}{2} m_{V,\rm ff} &= \frac{1}{2}(-2.5 \log L_{V,\rm ff}) + \text{ const.} \\ &= -2.5 \log(\dot{M}/v) + \text{ const.} \\ &= -2.5 \log L_{\gamma,\rm sh} + \text{ const.} \\ &= m_{\gamma,\rm sh} + \text{ const.}, \end{aligned} \tag{14}$$

so the slope of decay is different by a factor of 2. We plot the $m_{\gamma,\rm sh}$ (thin blue line labeled $\frac{1}{2}$ FF) in Figure 12(a), which represents the decay trend of GeV gamma-ray fluxes rather than the optical V flux itself.

5.5.2. Eddington Luminosity in the Fireball Stage

Munari et al. (2017) concluded that Phase I of Li et al. (2017; $t < 15$ days in Figure 12(a)) is the fireball stage of a nova. This means that we did directly observe the photosphere of the

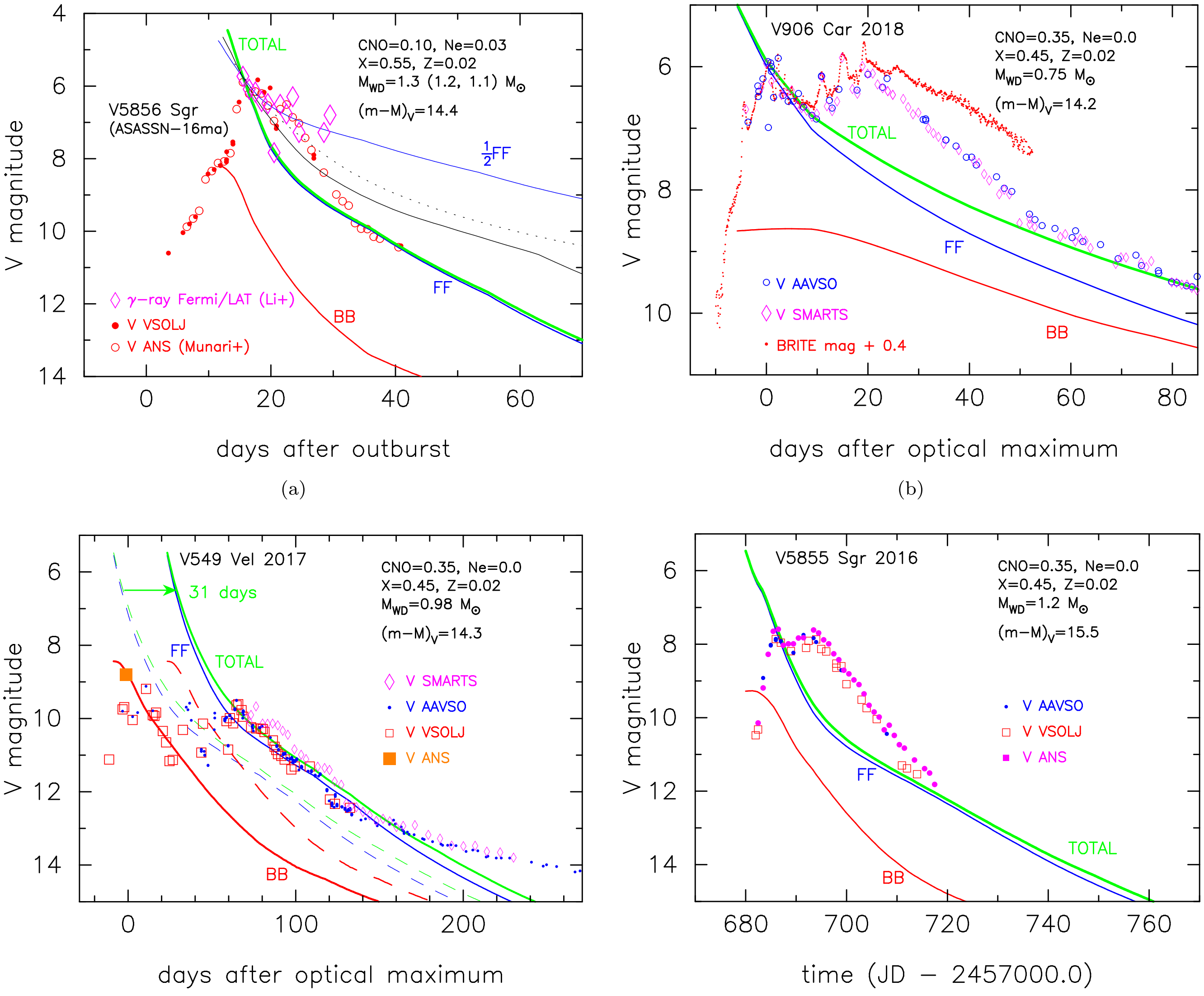

(a) (b)

(c) (d)

Figure 12. (a) Optical V magnitudes of the classical nova V5856 Sgr (ASASSN-16ma) are plotted on a linear timescale. The V data are taken from Munari et al. (2017) and the Variable Star Observers League of Japan (VSOLJ). We assume the V-band distance modulus of $(m-M)_V = 14.4$ to the nova. The red line denotes the blackbody emission from the photosphere (labeled BB) of a 1.3 $M_\odot$ WD (Ne2) model. The blue line is the free–free emission light curve (labeled FF) of the 1.3 $M_\odot$ WD. The green line corresponds to the total flux of FF and BB (labeled TOTAL) of the 1.3 $M_\odot$ WD. We added two other WD mass models of total V, 1.2 $M_\odot$ (thin solid black line) and 1.1 $M_\odot$ (thin dotted black line). We also added the gamma-ray fluxes observed with the Fermi/LAT (open magenta diamonds; Li et al. 2017) and half a slope of free–free emission light curve (thin blue line labeled $\frac{1}{2}$ FF). (b) V light curve of V906 Car. The optical V data are taken from AAVSO and SMARTS (Walter et al. 2012), and the BRITE data are from Aydi et al. (2020b). We assume $(m-M)_V = 14.2$. We fit a 0.75 $M_\odot$ WD (CO3) model to the V light curve. (c) The V light curve of V549 Vel. The optical V data are taken from SMARTS (Walter et al. 2012), AAVSO, and VSOLJ. The first peak ($V = 8.8$) is taken from ANS collaboration (filled orange squares; Li et al. 2020), and we set $t = 0$ day at this first V peak (MJD 58032.0). We assume $(m-M)_V = 14.3$. We fit a 0.98 $M_\odot$ WD (CO3) model to the V light curve. The first and second jitters are fitted with the red line labeled BB, while the last jitter and its decay phase are fitted with the green line labeled TOTAL, which is separated by 31 days from the first model light curve. See the text for more details. (d) V light curve of V5855 Sgr. The optical V data are taken from AAVSO, VSOLJ, and ANS (Munari et al. 2017). We assume $(m-M)_V = 15.5$. We adopt a 1.2 $M_\odot$ WD (CO3) model to fit it with the V light curve.

nova, so the observed magnitude is a direct result of the theoretical $L_{\rm ph}$, and not of the summation of $L_{\rm ph}$ and $L_{\rm ff}$. This occurs if free–free emission becomes dominant only after the optical peak, as suggested by Hachisu & Kato (2006). The sharp increase from $V \sim 8.4$ to $V \sim 6$ just before the optical maximum can be explained as a sudden increase in the free–free emission.

Our theoretical photospheric luminosity $L_{\rm ph}$, which is close to the Eddington limit, corresponds to the absolute V magnitude of $M_V \approx -6.2$. This value is converted to the apparent V magnitude of $m_V = (m-M)_V + M_V = 14.4 - 6.2 = 8.2$ at $t \sim 15$ day (the last days of Phase I). Figure 12(a) supports our interpretation that the V brightness jumps from the photospheric luminosity close to the Eddington limit to a phase dominated by free–free emission.

This is a possible theoretical explanation for the pre-maximum halt, which was already pointed out by Hachisu & Kato (2004). They proposed a relation between the WD mass and V brightness at the pre-maximum halt, i.e., $M_{V,\rm halt} \approx -1.75(M_{\rm WD}/M_\odot)$–4.25, for the chemical composition[5] of

---

[5] The photospheric Eddington luminosity, $L_{\rm Edd,\ ph} = 4\pi cGM_{\rm WD}/\kappa_{\rm ph}$, depends on the opacity at the photosphere, $\kappa_{\rm ph}$. The opacity is not only a function of T and ρ but also depends on the chemical composition.

C+O = 0.30 (CO2), which gives $M_V \sim -6.5$ for 1.3 $M_\odot$ WD (CO2), slightly brighter than our $M_V \sim -6.2$ for the chemical composition of Ne2.

To summarize, we directly observe the photosphere so that we get only the photospheric luminosity $L_{\rm ph}$ at the pre-maximum halt. After that, free–free emission dominates, and the luminosity can exceed the Eddington limit.

5.5.3. Shock Outside the Photosphere

Li et al. (2017) reported the P Cygni absorption profiles on Hα line in their Supplementary Figure 2. We adopted $v_{\rm p} = 800$ km s^{-1} and $v_{\rm d} = 2200$ km s^{-1}, as already obtained in Section 4.2.1. Then, the shocked thermal temperature is k$T_{\rm sh} = 2.0$ keV from Equation (3), which is high enough to emit hard ($\gtrsim$1 keV) X-rays. The shocked thermal energy generation rate is estimated to be $L_{\rm sh} = 1.8 \times 10^{37}(1.4)^3/2.2 \times 1.0 = 2.2 \times 10^{37}$ erg s^{-1} from Equation (5) for $\dot{M}_{\rm wind} = 1.0 \times 10^{-4}\, M_\odot$ yr^{-1} from our model light curve fitting.

GeV gamma rays were detected from +1 day to +14 day (after the optical maximum). The optical depth of gamma rays (∼GeV) is

$$\tau_\gamma \approx 8 \times 10^{-3}\left(\frac{\dot{M}_{\rm wind}}{10^{-4} M_\odot\ {\rm yr}^{-1}}\right)\left(\frac{r}{10^{13}\ {\rm cm}}\right)^{-1} \times \left(\frac{v_{\rm wind}}{400\ {\rm km\ s}^{-1}}\right)^{-1}\left(\frac{E_X}{300\ {\rm MeV}}\right)^{-1}, \tag{15}$$

which is taken from Equation (11) of Li et al. (2017). This is small enough for gamma rays to diffuse out from the shocked matter, even if we adopt $\dot{M}_{\rm wind} \sim 10^{-3}\, M_\odot$ yr^{-1} and $v_{\rm wind} \sim 4000$ km s^{-1} (see, e.g., Martin et al. 2018).

Li et al. (2017) estimated the GeV gamma-ray luminosity to be $L_\gamma \sim 1 \times 10^{36}$ erg s^{-1}, which gives the conversion rate to GeV gamma rays, $L_\gamma/L_{\rm sh} \sim 0.04$, in our shock model.

5.5.4. Hard X-Ray Emission

The ejecta mass is calculated to be $M_{\rm ej} = 0.25 \times 10^{-5}\, M_\odot$ from our 1.3 $M_\odot$ WD model. Then, we obtain the emergence time of hard X-rays of $t_{\rm H21} \sim 38$ days for $v_{\rm p} = 1000$ km s^{-1}. Here, the velocity of the principal system increased to $v_{\rm p} = 1100$ km s^{-1} 11 days after the optical maximum (see Supplementary Figure 2 of Li et al. 2017), so we adopt $v_{\rm p} = 1000$ km s^{-1} for an averaged value from -500 km s^{-1} to -1100 km s^{-1} for the principal system. If we set $N_{\rm H} \sim 10^{22}$ cm^{-2} for hard X-ray detection (Mukai & Ishida 2001), we have $t_{\rm H22} \sim 10$ days for $M_{\rm ej} = M_{\rm shell} \sim 0.15 \times 10^{-5}\, M_\odot$. However, no hard X-ray emission from ASASSN-16ma (V5856 Sgr) was detected with Swift/XRT both around the optical peak and five months later (Li et al. 2017). This is because the optical depth for hard X-rays is too large ($\tau_X \sim 10^3$) post-maximum, and optically thick winds had already stopped at $t \sim 74$ day after the optical maximum in our 1.3 $M_\odot$ WD (Ne2) model. In other words, the shock wave has already faded out before $t \sim 135$ day (∼five months) because the wind had stopped much earlier than this epoch. We will revisit the reason of no detection of hard and soft X-rays in Section 5.7.3 in more detail.

5.5.5. Optical Depth to a Shocked Layer

Optical depth to a shocked layer is estimated to be

$$\tau_{\rm opt} \approx 0.42\left(\frac{\dot{M}_{\rm wind}}{10^{-4} M_\odot\ {\rm yr}^{-1}}\right)\left(\frac{r}{10^{13}\ {\rm cm}}\right)^{-1} \times \left(\frac{v_{\rm wind}}{400\ {\rm km\ s}^{-1}}\right)^{-1}\left(\frac{\kappa_{\rm opt}}{0.1\ {\rm cm}^{-2}\ {\rm g}^{-1}}\right), \tag{16}$$

which is taken from Equation (7) of Li et al. (2017). Here, $\kappa_{\rm opt}$ is the opacity. If we adopt $v_{\rm wind} = 1000$ (or 400) km s^{-1} and a shock radius of $r \sim 10^{14}$ cm, we have $\tau_{\rm opt} \sim 10^{-2}$ (or $\sim 10^{-1}$). Thus, the shocked layer is always optically thin. In other words, we can always see the photosphere and inner wind through the shocked layer as illustrated in Figure 4.

5.6. Other Novae Detected in GeV Gamma Rays

What makes a nova observable in GeV gamma rays? Equation (5) gives a hint. The shocked energy flux depends on the velocity difference between $v_{\rm p}$ and $v_{\rm d}$ post-maximum as well as the wind mass-loss rate $\dot{M}_{\rm wind}$, which is the largest at the optical maximum and decreases afterward. In our steady-state optically thick wind model, the wind mass-loss rate near the optical peak is as large as (1–3) $\times 10^{-4} M_\odot$ yr^{-1} (see Figures 1, 7, and 10) and decreases afterwards. We regard that the decay in the gamma-ray flux is governed by the decrease in the wind mass-loss rate, as shown by the $\frac{1}{2}$ FF line in Figure 12(a), rather than by the decrease in the velocity difference $v_{\rm d} - v_{\rm p}$.

In this subsection, we analyze three novae, V906 Car, V549 Vel, and V5855 Sgr, whose ejecta velocities are well observed post-maximum. All the spectroscopic data are taken from Aydi et al. (2020a).

5.6.1. V906 Car 2018

V906 Car is a nova detected in GeV gamma rays (Aydi et al. 2020b). This nova shows a remarkable correlation between the optical and gamma-ray fluxes, like V5856 Sgr (Li et al. 2017; Aydi et al. 2020b).

Aydi et al. (2020b) estimated the distance and reddening to V906 Car to be $d \sim 4.0$ kpc and $A_V = 1.2$ mag (or $E(B-V) = A_V/3.1 = 0.4$ mag), respectively, so we have a distance modulus in the V band of $(m-M)_V = A_V + 5\log(d/10\ {\rm pc}) = 14.2$. Figure 12(b) shows the V light curve of V906 Car together with BRITE magnitudes, the data of which are taken from AAVSO, SMARTS, and Aydi et al. (2020b). The BRITE filter transmission is between 550 nm and 700 nm.

The optical spectra in an early phase were obtained by Aydi et al. (2020a). They presented the velocities of the deepest narrow P Cygni absorption lines on Hα, which increase from -210 km s^{-1} at the optical maximum (day 0) to -340 km s^{-1} 6 days after the maximum (day 6). We adopt these -210 km s^{-1} and -340 km s^{-1} as the velocities of the principal system post-maximum (at +0 day and +6 day, respectively). A broad absorption feature from -1800 km s^{-1} to -1200 km s^{-1} was observed at day 6 in the same Hα line. We assign this broad velocity feature to the velocity of the diffuse-enhanced system post-maximum (at +6 day). Substituting $v_{\rm p} = (210 + 340)/2 = 275$ km s^{-1} and $v_{\rm d} = (1800 + 1200)/2 = 1500$ km s^{-1} into

Equation (5), we obtain $L_{\rm sh} \sim 1.8 \times 10^{37} \times (1.23)^3/1.5 = 2.2 \times 10^{37}$ erg s^{-1} for $\dot{M}_{\rm wind} = 1 \times 10^{-4} M_\odot$ yr^{-1}.

Aydi et al. (2020b) estimated the GeV gamma-ray flux of V906 Car to be $L_\gamma \sim 1 \times 10^{36}$ erg s^{-1} from day 14 to day 34, which amounts to 5% of our shock luminosity $L_{\rm sh}$, i.e., $L_\gamma/L_{\rm sh} = 0.05$. They are no Fermi/LAT observations between day 0 and day 14 because Fermi/LAT was down.

It should be noted that we must increase the wind mass-loss rate from $\dot{M}_{\rm wind} \sim 1 \times 10^{-4} M_\odot$ yr^{-1} to $\dot{M}_{\rm wind} \sim 2 \times 10^{-3} M_\odot$ yr^{-1} or more if we take a ratio of $L_\gamma/L_{\rm opt} \sim 0.001$–$0.002$ and the shock luminosity covers all the optical luminosity, which amounts to $L_{\rm opt} \sim 10^{39}$ erg s^{-1}, as suggested by Li et al. (2017) and Aydi et al. (2020b). These estimates are based on the very good correlation between the gamma-ray and optical fluxes. Such a large mass-loss rate, however, challenges our optically thick wind model (Kato & Hachisu 1994).

Sokolovsky et al. (2020) reported the NuSTAR observation +24 and +45 days after the optical maximum. They obtained the temperature, $kT \sim 8.6$ keV and 4.4 keV, respectively, at day 24 and day 45, the hydrogen column density, $N_{\rm H} \sim 4.3 \times 10^{22}$ cm^{-2} and 0.6×10^{22} cm^{-2}. The Swift/XRT detected X-rays many times from day ~50 to day 440. The temperature of optically thin plasma decreases from several keV to a few tenths keV as well as the hydrogen column density from 0.6×10^{22} cm^{-2} to 0.01×10^{22} cm^{-2} (Sokolovsky et al. 2020).

We have estimated the hydrogen column density $N_{\rm H}$ at the two epochs. The shocked shell mass is $M_{\rm shell} = 0.85 \times 10^{-5} M_\odot$ (at day 24) and $M_{\rm shell} = 1.27 \times 10^{-5} M_\odot$ (at day 45) calculated from our $0.75 M_\odot$ model (it reached $M_{\rm shell} = 2.5 \times 10^{-5} M_\odot$ when the winds stopped). Substituting these values together with the shell velocity (=shock velocity) of $v_{\rm p} = 420$ km s^{-1} (at day 16.5 in Figure 11 of Aydi et al. 2020a) and $v_{\rm p} \sim 760$ km s^{-1} (at day 40, linear extrapolation from their Figure 11) into Equation (11), we obtain $N_{\rm H} \sim 4.8 \times 10^{22}$ cm^{-2} at day 24 and 0.63×10^{22} cm^{-2} at day 45, being broadly consistent with Sokolovsky et al. (2020)'s values.

We have estimated $kT_{\rm sh} \approx ((1800 - 340)/1000)^2 \sim 2$ keV at day 6 from Equation (3) by using the higher-velocity component of the diffuse-enhanced system. This value is much lower than their estimates based on the NuSTAR data, but consistent with the temperature based on the Swift data between day 168 and day 238 (Sokolovsky et al. 2020).

Our 0.75 $M_\odot$ WD model predicts the wind duration of $t_{\rm wind} \sim 720$ days and the hydrogen shell burning up to ~2360 days, although these durations depend on the chemical composition of the envelope, X and $X_{\rm CNO}$. If this is the case, supersoft X-ray emission emerges about two years after the outburst and continues up to 6.5 years after the outburst at a rate of $L_{\rm ph} \sim 7 \times 10^{37}$ erg s^{-1} and $kT_{\rm ph} \sim 40$ eV (Kato & Hachisu 1994; Hachisu & Kato 2006, 2010).

5.6.2. V549 Vel 2017

V549 Vel is also a nova detected in GeV gamma rays (Li et al. 2020). Figure 12(c) shows the V light curve of V549 Vel as well as a 0.98 $M_\odot$ WD (CO3) model light curve. We assume that the V-band distance modulus is $(m - M)_V = A_V + 5 \log(d/10 \text{ pc}) = 3.1 \times E(B - V) + 11.15 = 14.3$, where we adopt $d = 1.7$ kpc from Gaia EDR3 (Bailer-Jones et al. 2021) and $E(B - V) = 1.0$ mag from Li et al. (2020). This nova experienced four jitters through maximum light (see Figure 2 of Li et al. 2020).

We fit our photospheric V (thick solid red line, labeled BB) magnitudes with the first and second jitters and its decay. For the last jitter (fourth), we apply the total V (thick solid green, labeled TOTAL, i.e., BB+FF) light curve. This is because free–free emission from plasma outside the photosphere does not yet dominate the spectrum in the very early phase, and we directly observed the photosphere (Li et al. 2020). Free–free emission dominates the spectra only after a large amount of gas has been eventually ejected during the four jitters.

The first V peak ($V = 8.8$) is reached at MJD 58032.0 (ANS collaboration data denoted by the filled orange squares; Li et al. 2020) about 11 days before the second V peak (MJD 58043.4; Aydi et al. 2020a). We set $t = 0$ day at this first V peak (MJD 58032.0), although Aydi et al. (2020a) assumed that the second V peak of $V = 9.0$ was the optical maximum.

Aydi et al. (2020a) obtained the velocity of the deepest narrow Hα P Cygni absorption line, from -1000 km s^{-1} at day -7.5 (7.5 days before the optical maximum), -700 km s^{-1} at day -2, -600 km s^{-1} at day $+3$, i.e., the velocity decreases toward the optical maximum, and then increases to -800 km s^{-1} at day $+53$. We adopt this velocity as the principal system. Thus, we obtain the velocity of the principal system post-maximum, $v_{\rm p} \approx 800$ km s^{-1}. On the other hand, we can see a shallow absorption trough between -2700 and -2200 km s^{-1} in Hα P Cygni profile on day +53. We attribute this absorption to the diffuse-enhanced system. Then we have a velocity of $v_{\rm d} = (2700 + 2200)/2 = 2450$ km s^{-1} post-maximum.

The temperature just behind the shock is estimated to be $k\ T_{\rm sh} \approx ((2450$–$800)/1000)^2 = 2.7$ keV from Equation (3). The thermal energy generation rate at the shock is given by Equation (5), and we obtain $L_{\rm sh} \approx 1.8 \times 10^{37}$erg s^{-1} $((2450 - 800)/1000)^3(1000/2450) \times 0.5 = 1.7 \times 10^{37}$ erg s^{-1} for $\dot{M}_{\rm wind}$=0.5 $\times 10^{-4} M_\odot$ yr^{-1} from fitting.

Hard X-rays were detected with Swift from 42 days after the maximum, and soft X-ray emission emerged from 222 days after the maximum (Li et al. 2020; Page et al. 2020). The plasma temperature of hard X-ray emission was estimated to be 1–2 keV, which is consistent with our analysis from the velocity difference of $v_{\rm d} - v_{\rm p}$.

The emergence time of hard X-ray emission is estimated from Equation (12). Li et al. (2020) obtained a hydrogen column density of $N_{\rm H} \sim 9.5^{+2.9}_{-2.7} \times 10^{21}$ cm^{-2}. We obtain an ejecta mass of $M_{\rm ej} = 1.1 \times 10^{-5} M_\odot$ from our model light curve fitting in Figure 12(c). The velocity of the shock is $v_{\rm shock} = v_{\rm p} = (600 + 800)/2 = 700$ km s^{-1} from the principal absorption system in V549 Vel (Aydi et al. 2020a). Substituting these two values into Equation (12), we have $t_{\rm H22} \sim 40$ day for $N_{\rm H} \sim 10^{22}$ cm^{-2}. This is broadly consistent with the hard X-ray emergence time $t \sim 42$ days after the optical maximum (Li et al. 2020).

The photosphere shrinks, and the photospheric temperature increases high enough to emit supersoft X-rays only after the optically thick winds stop (Kato & Hachisu 1994; Hachisu & Kato 2006, 2010). The wind duration is $t_{\rm wind} \sim 250$ days in our 0.98 $M_\odot$ WD (CO3) model, being broadly consistent with the emergence of soft X-ray emission from 222 days after the maximum (Li et al. 2020; Page et al. 2020). The internal absorption by the shocked ejecta is estimated from the hydrogen column density $N_{\rm H}$ (Equation (11)) to be about $N_{\rm H} \sim 2 \times 10^{20}$ cm^{-2} at $t \sim 220$ day, low enough for soft X-rays to diffuse out.

GeV gamma-ray emissions were also detected with Fermi/LAT from day +5 to day +38 (Li et al. 2020), that is, gamma-ray emission appears several days after the optical maximum.

Li et al. (2020) pointed out that there is no clear correlation between optical flux and gamma-ray flux. Such uncorrelation is a remarkable contrast to the excellent correlation in V5856 Sgr and V906 Car (Li et al. 2017; Aydi et al. 2020b). Li et al. (2020) also estimated the GeV gamma-ray flux to be $L_\gamma \sim 4 \times 10^{33}$ erg s^{-1} for the distance to the nova of $d = 560$ pc. If we adopt $d = 1.7$ kpc from Gaia EDR3 (Bailer-Jones et al. 2021), we have $L_\gamma \sim 4 \times 10^{34}$ erg s^{-1}, about 10 times larger, being consistent with those in the low L_γ group (∼a few to several 10^{34} erg s^{-1}, e.g., Li et al. 2020).

Li et al. (2020) obtained the ratio of $L_\gamma / L_{\mathrm{opt}} \approx 0.1\%$. Then, we have $L_{\mathrm{opt}} \sim 4 \times 10^{37}$ erg s^{-1}, which is a half of the photospheric luminosity of our 0.98 $M_\odot$ WD model, i.e., $L_{\mathrm{ph}} \sim 8.5 \times 10^{37}$ erg s^{-1} at the optical maximum ($M_V \sim -5.5$,filled orange square in Figure 12(c), Li et al. 2020). A majority of luminosity comes from the photosphere because the shocked thermal energy generation rate (a few 10^{37} erg s^{-1}) is smaller than the photospheric luminosity ($\sim 9 \times 10^{37}$ erg s^{-1}). This is the reason why there is no clear correlation between optical flux and GeV gamma-ray flux.

Thus, our shock model based on a 0.98 $M_\odot$ WD (CO3) model is consistent with the observation.

5.6.3. V5855 Sgr 2016

GeV gamma rays were detected in V5855 Sgr by Fermi/LAT (Nelson et al. 2019). Figure 12(d) shows the V light curve of V5855 Sgr and our 1.2 $M_\odot$ WD (CO3) model light curve fitting. Here, we assume the V-band distance modulus of $(m - M)_V = A_V + 5 \log(d/10 \text{ pc}) = 3.1 \times E(B - V) + 14.23 = 15.5$. Both the distance of $d = 7.0$ kpc and reddening of $E(B - V) = 0.42$ mag are taken from Munari et al. (2017). Shifting horizontally our model V light curve (green, labeled TOTAL), we place the green line on the first V peak ($V = 7.6$). The model V light curve does not follow the observation in the middle phase but approaches the observation in the last part. This trend is very similar to those of V5856 Sgr and V906 Car.

Aydi et al. (2020a) obtained the velocities of deepest narrow Hα P Cygni absorption lines, from -250 km s^{-1} at day -1.4 (1.4 days before the optical maximum) to -600 km s^{-1} at day $+1.5$. They also showed a shallow broad absorption feature from -3200 to -2500 km s^{-1} and a deepest narrow absorption at -700 km s^{-1} on Hα line at day $+7.2$. If we adopt $v_{\mathrm{d}} = (3200 + 2500)/2 = 2850$ km s^{-1} and $v_{\mathrm{p}} = 700$ km s^{-1}, the thermal temperature just behind the shock is $\mathrm{k}T_{\mathrm{sh}} = 2.1$ keV from Equation (3) and the shocked thermal energy generation rate is $L_{\mathrm{sh}} = 1.8 \times 10^{37} \times (2.15)^3/2.85 = 6.3 \times 10^{37}$ erg s^{-1} for $\dot{M}_{\mathrm{wind}} = 1 \times 10^{-4} M_\odot$ yr^{-1}, from Equation (5). The absolute V magnitude at the peak is estimated to be $M_V = m_V - (m - M)_V = 7.6 - 15.5 = -7.9$, which gives the wind mass-loss rate of $\dot{M}_{\mathrm{wind}} = 1.6 \times 10^{-4} M_\odot$ yr^{-1} and the total ejecta mass of $M_{\mathrm{shell}} = 0.35 \times 10^{-5} M_\odot$ on our 1.2 $M_\odot$ WD model (see, e.g., Hachisu et al. 2020).

Nelson et al. (2019) obtained the GeV gamma-ray flux[6] of $L_\gamma \sim 7 \times 10^{35} (d/4.5 \text{ kpc})^2$ erg s^{-1}, 7–15 days after discovery (discovery day = JD 2457681.883). If we adopt $d = 7$ kpc from Munari et al. (2017), this reads $L_\gamma \sim 1.7 \times 10^{36}$ erg s^{-1}, which is similar to that of V5856 Sgr. Then the conversion rate to gamma-ray is about 2%–3%, i.e., $L_\gamma / L_{\mathrm{sh}} = 0.02$–$0.03$.

Nelson et al. (2019) obtained hard X-ray emission from V5855 Sgr with NuSTAR 15 days after discovery, but did not detect four days later. Their analyzed results show that $N_{\mathrm{H}} = 2.2 \times 10^{24}$ cm^{-2}, k $T = 11$ keV, $L_{\mathrm{X}} = 8 \times 10^{35} (d/4.5 \text{ kpc})^2$ erg s^{-1}. If we assume $d = 7$ kpc, this reads $L_{\mathrm{X}} = 2 \times 10^{36}$ erg s^{-1}. We obtain the hydrogen column density of $N_{\mathrm{H}} \approx 4 \times 20^{22}$ cm^{-2} from Equation (11), and the shock energy generation rate of $L_{\mathrm{sh}} = 6 \times 10^{37}$ erg s^{-1} as calculated above. Then the conversion rate to X-ray is about 3%, i.e., $L_{\mathrm{X}} / L_{\mathrm{sh}} = 0.03$.

The ratio of hard X-ray to gamma-ray is almost unity, i.e., $L_{\mathrm{X}} / L_\gamma \sim 1$, for this nova, which is very unusual among various GeV gamma-ray detected novae because Gordon et al. (2021) showed a relation of $L_\gamma \sim (10^2$–$10^3) L_{\mathrm{X}}$. We believe that this small ratio of X-rays to gamma rays, $L_{\mathrm{X}} / L_\gamma \sim 0.01$, comes mainly from the quick decrease in the wind mass-loss rate $\dot{M}_{\mathrm{wind}}$. When hard X-ray emission emerges in a mid or later phase, $\dot{M}_{\mathrm{wind}}$ had already decreased down to $\lesssim 10^{-5} M_\odot$ yr^{-1} or less. Thus, L_{sh} had decreased to much smaller than that of GeV gamma rays because L_{sh} is proportional to $\dot{M}_{\mathrm{wind}}$.

Our 1.2 $M_\odot$ WD (CO3) model predicts the wind duration of $t_{\mathrm{wind}} \sim 95$ days and hydrogen shell burning duration of $t_{\mathrm{Hburn}} \sim 162$ days. The so-called supersoft X-ray (k $T \lesssim 100$ eV) source phase starts after optically thick winds stop (Hachisu & Kato 2006, 2010) and ends after hydrogen shell burning stops. Soft X-ray (0.3–1.0 keV) emission was once observed with Swift 150 days after discovery (Gordon et al. 2021). This epoch is in the period of supersoft X-ray source (SSS) phase because optically thick winds had stopped in our model ($t_{\mathrm{wind}} \sim 95$ days) but hydrogen is still burning ($t_{\mathrm{Hburn}} \sim 162$ days).

5.6.4. GeV Gamma-ray Detectability in Novae

We have analyzed several gamma-ray novae with rich optical information in previous sections. We may draw common properties for gamma-ray novae having a red dwarf companion. GeV gamma-ray emission could be detected with Fermi/LAT in such a nova that satisfies

1. $v_{\mathrm{d}} - v_{\mathrm{p}} = v_{\mathrm{wind}} - v_{\mathrm{shock}} \gtrsim 1000$ km s^{-1}
2. $\dot{M}_{\mathrm{wind}} \gtrsim 1 \times 10^{-4} M_\odot$ yr^{-1}
3. A relatively small distance to a nova, possibly $d \lesssim 6 - 7$ kpc (e.g., Franckowiak et al. 2018; Gordon et al. 2021).

5.7. Emergence of Hard X-Rays in GeV Gamma-ray Novae

The above conditions for GeV gamma-ray emission are all necessary conditions for hard X-ray detection. We should further add a condition, that the hydrogen column density decreases to $N_{\mathrm{H}} \sim 10^{21}$ cm^{-1} before continuous wind stops. If we define this time as t_{H21} from Equation (12) and the wind stopping time as t_{wind}, this reads $t_{\mathrm{H21}} \lesssim t_{\mathrm{wind}}$. If we include the retarded (look back) time as discussed in Section 4.1, this correctly reads $t_{\mathrm{H21}} \lesssim t_{\mathrm{wind}} + t_{\mathrm{ret}}$, where $t_{\mathrm{ret}} = (R_{\mathrm{sh}}(t) - R_{\mathrm{ph}}(t - t_{\mathrm{ret}}))/v_{\mathrm{ph}}(t - t_{\mathrm{ret}})$. With another relation of $(t_{\mathrm{wind}} + t_{\mathrm{ret}}) v_{\mathrm{p}} \sim v_{\mathrm{d}} t_{\mathrm{ret}}$, the condition is rewritten as

$$t_{\mathrm{H21}} \lesssim t_{\mathrm{wind}} \Big/ \left(1 - \frac{v_{\mathrm{p}}}{v_{\mathrm{d}}}\right). \tag{17}$$

We further simplify this condition to

$$t_{\mathrm{H21}} \lesssim 2\, t_{\mathrm{wind}} \tag{18}$$

---

[6] In their original text, $L_\gamma \sim 7 \times 10^{35} (d/4.5 \text{ kpc})$ erg s^{-1}. We add the power of 2 in the distance dependency.

with a broad relation of $v_{\rm d} \sim 2v_{\rm p}$ (McLaughlin 1942). This also requires the observing epoch ($t_{\rm hX}$) of

$$t_{\rm H21} \lesssim t_{\rm hX} \lesssim t_{\rm wind} \bigg/ \left(1 - \frac{v_{\rm p}}{v_{\rm d}}\right), \tag{19}$$

or simply,

$$t_{\rm H21} \lesssim t_{\rm hX} \lesssim 2\, t_{\rm wind}, \tag{20}$$

for hard X-ray detection.

Gordon et al. (2021) discussed the relation between hard X-ray detected novae and GeV gamma-ray detected novae. Here, we simply assume that all GeV gamma-ray novae emit hard X-rays and these hard X-rays could be detected if Equation (19) or Equation (20) is satisfied. Actually, hard X-ray emission was observed in GeV gamma-ray novae, mostly detected but two exceptions, V1324 Sco and V5856 Sgr. No detection of hard X-rays are due either to the lack of observation at proper $t_{\rm hX}$ in Equation (19) or to no proper $t_{\rm hX}$ times in Equation (19). For example, if circumstellar or interstellar $N_{\rm H}$ is larger than a few times 10^{22} cm^{-2} or more, we obtain $t_{\rm H21} = \infty$, that is, $t_{\rm H21} \gtrsim t_{\rm wind} \bigg/ \left(1 - \frac{v_{\rm p}}{v_{\rm d}}\right)$ in Equation (19) and we have no detection of hard X-rays.

5.7.1. Observability of Hard X-ray Emission

The condition (19) means that hard X-rays are observable only after the hydrogen column density decreases to about $N_{\rm H} \sim 10^{21}$ cm^{-1} but before the shock fades out, in other words, before the last wind collides with the shock. In V1974 Cyg, we have $t_{\rm H21} = 61$ day and $t_{\rm wind} = 250$ day from our 0.98 $M_\odot$ WD (CO3) model. These values satisfy the condition, i.e., Equations (19) or (20).

5.7.2. Concurrent Detection of Hard and Supersoft X-ray Emissions

The so-called supersoft X-ray (k $T \lesssim 100$ eV) source phase of a nova starts after optically thick winds stop, that is, $t \gtrsim t_{\rm wind}$ (e.g., Hachisu & Kato 2006, 2010). It should be noted that hard X-ray emission is detected even during the supersoft X-ray source phase because its duration extends up to $\sim t_{\rm wind} \bigg/ \left(1 - \frac{v_{\rm p}}{v_{\rm d}}\right)$ or simply $\sim 2\, t_{\rm wind}$. In V959 Mon, hard X-ray emission was always observed during the supersoft X-ray source phase (e.g., Page et al. 2013; Hachisu & Kato 2018a).

5.7.3. V5856 Sgr 2016

We discuss the reason why no hard X-ray emission was detected in V5856 Sgr. The Swift satellite observed V5856 Sgr twice, +1 day and +135 day after the optical maximum. At the first observation the hydrogen column density was too large to detect hard X-rays. In our model the wind stopped at $t_{\rm wind} \sim 74$ day which gives $t_{\rm wind}/(1\text{–}1000/2200) = 136$ day in Equation (19). This is very close to the second observation epoch $t_{\rm hX} \sim 135$ day. Thus, the wind could have stopped and shock has already disappeared, or even if the shock still survived, the shock luminosity has decreased as low as $L_{\rm sh} \lesssim 1 \times 10^{34}$ erg s^{-1}, because the wind mass-loss rate decreased to $\dot{M}_{\rm wind} \lesssim 1 \times 10^{-7}\, M_\odot$ yr^{-1}.

It has been argued that observed hard X-ray luminosity is orders of magnitude smaller than that theory expects (Nelson et al. 2019; Sokolovsky et al. 2020). If we apply this argument to V5856 Sgr, the upper limit of $L_X \lesssim 4 \times 10^{32}$ erg s^{-1} at +135 day obtained by Li et al. (2017) is consistent with the upper limit on the shock model luminosity, $L_{\rm sh} \lesssim 1 \times 10^{34}$ erg s^{-1} (+135 day) with $L_{\rm X}/L_{\rm sh} \lesssim 0.03 L_{\rm X}/L_\gamma \lesssim 0.03 \times 0.01 \sim 10^{-4}$.

Supersoft X-ray emission is observable only after the optically thick winds stop. This is because the photosphere shrinks, and the photospheric temperature becomes high enough to emit supersoft (< 100 eV) X-rays at a rate of $L_X \sim 10^{38}$ erg s^{-1} (Ogelman et al. 1993; Krautter et al. 1996; Kahabka & van den Heuvel 1997; Kato 1997; Hachisu & Kato 2006, 2010; Schwarz et al. 2011). In our 1.3 $M_\odot$ WD model, hydrogen shell burning had ended at +117 day. Thus, the second observation epoch (+135 day) with Swift is possibly too late to detect both hard and soft X-rays.

5.7.4. V1324 Sco 2012

Finzell et al. (2018) reported the P Cygni absorption profile on Hα line in V1324 Sco, the velocities of which are roughly measured to be -900 km s^{-1} (at +3 day, 2012 June 1st = JD 2456079.5 = +0 day), -700 km s^{-1} (+7 day), -600 km s^{-1} at the first optical maximum (+13 day), -600 km s^{-1} (+17 day), -800 km s^{-1} (+19 day). Thus, we obtain the velocity of the principal system, $v_{\rm p} \sim 800$ km s^{-1}, post-maximum. Finzell et al. (2018) reported that the higher-velocity component appeared a few weeks later and reached 2600 km s^{-1}. They also reported a slower component of 1000 km s^{-1} at the same day. GeV gamma rays were detected from +14 day (+1 day after the optical maximum) to +29 day (+16 days after the maximum). If we regard that $v_{\rm p} = 800$ km s^{-1} and $v_{\rm d} = 2600$ km s^{-1}, the shocked thermal temperature is k$T_{\rm sh} = 3$ keV from Equation (3), which is high enough to emit hard (2–3 keV) X-rays. The shocked thermal energy generation rate is estimated to be $L_{\rm sh} = 1.8 \times 10^{37} (1.8)^3/2.6 = 4 \times 10^{37}$ erg s^{-1} from Equation (5) for $\dot{M}_{\rm wind} = 1 \times 10^{-4}\, M_\odot$ yr^{-1}.

We obtain the ejecta mass of $M_{\rm ej} = 2.2 \times 10^{-5}\, M_\odot$ from the light curve fitting with a 0.8 $M_\odot$ WD (CO2; Hachisu & Kato 2019b). The model predicts the wind duration of $t_{\rm wind} = 490$ day. Equation (12) gives $t_{\rm H21} \sim 140$ day. The Swift satellite observed V1324 Sco two times, +355 and +520 day, so that these two observing epochs satisfy the Equations (19) or (20). However, no hard or soft X-rays have been detected with Swift (Finzell et al. 2018).

Soft X-rays are possibly not detected due to a large interstellar extinction of $E(B-V) = 1.32$ mag (e.g., Hachisu & Kato 2018b, 2019b, 2021), corresponding to $N_{\rm H} = 8.3 \times 10^{21} \times E(B-V) = 1.1 \times 10^{22}$ cm^{-2} based on the relation of Liszt (2014). In this sense, there may not be a proper time of $t_{\rm hX}$ satisfying Equation (19) for hard X-rays because always $N_{\rm H} \gtrsim$ a few times 10^{22} cm^{-2}.

Moreover, this nova experienced a deep dust blackout, as deep as 10 mag in the optical band, from +45 day to +147 day. The last day of the dust blackout is close to our $t_{\rm H21} \sim 140$ day. For a possible solution to this mystery, Finzell et al. (2018) discussed that dust is a signature of the thermal shock, which quickly cools down by emitting high-energy (X-ray) photons that are absorbed by dense matter in the shell, which are finally reemitted in the optical or infrared (Derdzinski et al. 2017). This may be supported by a relatively massive shell ($M_{\rm shell}$ = a few to several times $10^{-5}\, M_\odot$) and slow expansion velocity of the shocked shell ($v_{\rm p} \lesssim 1000$ km s^{-1}). For such a deep dust blackout case, our simple $N_{\rm H}$ model of Equations (11) and (12) may not apply to V1324 Sco, at least, after the dust blackout started.

On the other hand, Gordon et al. (2021) pointed out that no detection of hard X-rays in V1324 Sco is due to its large distance ($d \gtrsim 6.5$ kpc). The distance to V1324 Sco was estimated by Hachisu & Kato (2018b, 2019a, 2021) to be $d = 3.7 \pm 0.4$ kpc together with the extinction of $E(B-V) = 1.32$ mag based on the color–magnitude diagram method and time-stretching method. The distance is also obtained by Bailer-Jones et al. (2021) to be $d = 4.9^{+1.9}_{-1.7}$ kpc based on the Gaia EDR3 parallax. Thus, the distance to V1324 Sco is much smaller than 6.5 kpc, so we may exclude the reason of a large distance to V1324 Sco.

To summarize, we may conclude that no detection of hard X-rays is due to a large absorption by dense matter of the shocked shell or high column density of the interstellar hydrogen, or both. In other words, there is no proper $t_{\rm hX}$ time that satisfies Equation (19).

5.8. Steady Versus Violent Mass Ejection

A remarkable difference is found in the light curves of novae between V382 Vel (Figure 9) and V5856 Sgr (Figure 12(a)). The light curve of V382 Vel well follows the 1.2 $M_\odot$ model light curve. On the other hand, V5856 Sgr has a wavy plateau above the model light curve, indicating violent vibration or multiple ejections just after the optical maximum. We dubbed the former case "steady (mass) ejection" and the latter case "violent (mass) ejection." We do not know what makes the difference.

Kato & Hachisu (2009, 2011) proposed a hypothesis of transition between two types of nova envelope solutions. One is a hydrostatic solution without winds, and the other is a steady-state wind solution. There is a large structure difference between them. The static solution could be perturbed by the companion star orbiting in the expanded WD envelope. So the static envelope changes its configuration toward the steady-wind solution (Kato & Hachisu 2011, for more detail). Violent activities are regarded as a relaxation process of transition from a static configuration to a wind solution. This can be applied to low-mass WDs ($M_{\rm WD} \lesssim 0.6$–$0.7\ M_\odot$).

Aydi et al. (2020b) proposed a complex density structured circumbinary torus to explain multiple peaks for V906 Car. Slow winds form circumstellar torus before the optical maximum, which has a complex density structure. After that, fast nova winds slam into the multiple high-density regions in the torus and makes multiple optical peaks. These brightening processes occur far outside the photosphere and have no effect on the outburst mechanism on the WD. Therefore, the light curve eventually approaches the steady-state trend of the nova light curve, as shown in Figures 12(a), 12(b), and 12(d), after the blast wave (forward shock) has broken out of the torus.

On the other hand, V549 Vel could be a case of transition between the two types of nova envelope solutions, although the WD mass (0.98 $M_\odot$) is somewhat larger than the mass range theoretically expected ($0.6-0.7\ M_\odot$). The first expansion seems to have no strong winds because its V light curve almost follows the photospheric (labeled BB, solid red line) luminosity in Figure 12(c), but the final outburst 31 days after the first outburst seems to follow the total flux (of free–free (FF) emission plus photospheric (BB) emission) light curve (labeled TOTAL, solid green line = FF (blue) + BB (dashed red line)), which shows strong winds.

We categorize a nova that shows a large excess in an early phase from our smooth decline model light curve as the group of violent ejection. Many of the novae that are detected in GeV gamma rays are classified into the group of violent ejection. For example, V339 Del shows a wavy structure similar to V5856 Sgr in the post-maximum phase (e.g., Skopal et al. 2014). V1369 Cen, V5668 Sgr, V1324 Sco, V5855 Sgr, V549 Vel, and V906 Car displayed multiple peaks (Cheung et al. 2016; Finzell et al. 2018; Aydi et al. 2020a).

These hydrodynamical phenomena are difficult to be involved in our 1D theoretical work because, in our time-dependent calculation, the envelope approaches a steady state after the optical maximum and shows no signature of a wavy behavior.

6. Conclusions

We propose a shock model in classical novae that can be responsible for absorption/emission line systems and hard X-ray emissions based on a fully self-consistent nova outburst model calculated by Kato et al. (2022a). Our main conclusions are as follows:

1. We explained that a shock is inevitably generated outside the photosphere. The wind velocity at the photosphere decreases with time before the optical maximum but increases afterward. This is the result of the evolution calculation by Kato et al. (2022a). Simply assuming ballistic loci of winds outside the photosphere, we followed the motion of fluid (wind) and obtained a strong shock formation soon after the optical maximum.
2. Increasing the wind velocity, from a few hundred to a thousand km s^{-1}, results in strong compression of gas. Thus, a strong shock (reverse shock) arises soon after the optical maximum. The velocity of the shocked matter ($v_{\rm shock}$) is a few hundred km s^{-1} smaller than that of the upstream wind ($v_{\rm wind}$), i.e., $v_{\rm wind} - v_{\rm shock} \sim (2$–$3) \times 100$ km s^{-1}.
3. A nova ejecta is divided by the shock into three parts: the outermost expanding gas (earliest wind before maximum), shocked shell, and inner fast wind. These three parts are responsible for pre-maximum, principal, and diffuse-enhanced absorption/emission line systems, respectively. A large part of nova ejecta are eventually confined to the shocked shell. The appearance of the principal system is consistent with the emergence of the shock.
4. We interpret that the shock velocity $v_{\rm shock}$ is the velocity $v_{\rm p}$ of the principal system, and the inner wind velocity $v_{\rm wind}$ is the velocity $v_{\rm d}$ of the diffuse-enhanced system. If we take the observed velocities of $v_{\rm d} - v_{\rm p}$ instead of our model values of $v_{\rm wind} - v_{\rm shock}$, the shocked layer has a high temperature of $kT_{\rm sh} \sim 1$ keV $((v_{\rm wind} - v_{\rm shock})/1000\ {\rm km\ s^{-1}})^2 = 1$ keV $((v_{\rm d} - v_{\rm p})/1000\ {\rm km\ s^{-1}})^2$, where $v_{\rm d} - v_{\rm p}$ is the velocity difference between the diffuse-enhanced ($v_{\rm d}$) and principal ($v_{\rm p}$) systems. This high temperature explains the hard X-ray emission from novae. The shocked matter becomes as hot as a few times 10^7 K and emits thermal X-rays in the keV range, because the velocity difference is usually $v_{\rm d} - v_{\rm p} \gtrsim 1000$ km s^{-1} in fast novae.
5. The shock arises after the optical maximum, so that hard (keV) X-ray emission could be detected after the optical maximum if its optical depth becomes small.

6. Our shock model also explains GeV gamma-ray emissions from classical novae based on Fermi acceleration of particles (proton–proton collisions at the shock). The shocked luminosity depends not only on the velocity difference, $v_{\rm d} - v_{\rm p}$, but also on the wind mass-loss rate, $\dot{M}_{\rm wind}$. Because $\dot{M}_{\rm wind}$ is the largest at the optical maximum and quickly decreases afterward, GeV gamma-ray emission is bright enough to be detected just in the post-maximum phase. Then, it quickly decays with decreasing $\dot{M}_{\rm wind}$.
7. Thus, we strongly recommend high-resolution spectroscopic observations of novae, in particular, before/after the optical maximum as well as in the post-maximum phase. These are essential to clarify the intrinsic nature of shocks in nova ejecta.

We thank the American Association of Variable Star Observers (AAVSO) and the Variable Star Observers League of Japan (VSOLJ) for the archival data of V1668 Cyg, V1974 Cyg, V382 Vel, V5855 Sgr, V549 Vel, and V5856 Sgr. We are also grateful to the anonymous referee for his/her useful comments, which helped improve the manuscript.

ORCID iDs

Izumi Hachisu https://orcid.org/0000-0002-0884-7404
Mariko Kato https://orcid.org/0000-0002-8522-8033

References

Abdo, A. A., Ackermann, M., Ajello, M., et al. 2010, Sci, 329, 817
Ackermann, M., Ajello, M., Albert, A., et al. 2014, Sci, 345, 554
Arai, A., Kawakita, H., Shinnaka, Y., & Tajitsu, A. 2016, ApJ, 830, 30
Aydi, E., Chomiuk, L., Izzo, L., et al. 2020a, ApJ, 905, 62
Aydi, E., Sokolovsky, K. V., Chomiuk, L., et al. 2020b, NatAs, 4, 776
Balman, S., Krautter, J., & Ogelman, H. 1998, ApJ, 499, 395
Bailer-Jones, C. A. L., Rybizki, J., Fouesneau, M., Demleitner, M., & Andrae, R. 2021, AJ, 161, 147
Cassatella, A., Lamers, H. J. G. L. M., Rossi, C., Altamore, A., & Gonzalez-Riestra, R. 2004, A&A, 420, 571
Chen, H.-L., Woods, T. E., Yungelson, L. R., et al. 2019, MNRAS, 490, 1678
Cheung, C. C., Jean, P., Shore, S. N., Grove, J. E., & Leising, M. 2015, ICRC, 34, 880
Cheung, C. C., Jean, P., Shore, S. N., et al. 2016, ApJ, 826, 142
Cheung, C. C., Ciprini, S., Johnson, T. J., et al. 2021a, ATel, 14834, 1
Cheung, C. C., Johnson, T. J., Mereu, I., et al. 2021b, ATel, 14845, 1
Chochol, D., Grygar, J., Pribulla, T., et al. 1997, A&A, 318, 908
Chochol, D., Hric, L., Urban, Z., et al. 1993, A&A, 277, 103
Chochol, D., Shugarov, S., Katysheva, N., & Volkov, I. 2015, in Proceedings of The Golden Age of Cataclysmic Variables and Related Objects—III (Golden2015) (Trieste: SISSA), 56, http://pos.sissa.it/cgi-bin/reader/conf.cgi?confid=255
Chomiuk, L., Linford, J. D., Yang, J., et al. 2014, Natur, 514, 339
Chomiuk, L., Metzger, B. D., & Shen, K. J. 2021, ARA&A, 59, 48
Della Valle, M., & Izzo, L. 2020, A&ARv, 28, 3
Della Valle, M., Pasquini, L., Daou, D., & Williams, R. E. 2002, A&A, 390, 155
Denissenkov, P. A., Herwig, F., Bildsten, L., & Paxton, B. 2013, ApJ, 762, 8
Derdzinski, A. M., Metzger, B. D., & Lazzati, D. 2017, MNRAS, 469, 1314
Duerbeck, H. W., Rindermann, R., & Seitter, W. C. 1980, A&A, 81, 157
di Paolantonio, A., Patriarca, R., & Tempesti, P. 1981, IBVS, 1913, 1
Ederoclite, A. 2014, in ASP Conf. Ser. 490, Stella Novae: Past and Future Decades, ed. P. A. Woudt & V. A. R. M. Ribeiro (San Francisco, CA: ASP), 163
Ennis, D., Beckwith, S., Gatley, I., et al. 1977, ApJ, 214, 478
Epelstain, N., Yaron, O., Kovetz, A., & Prialnik, D. 2007, MNRAS, 374, 1449
Finzell, T., Chomiuk, L., Metzger, B. D., et al. 2018, ApJ, 852, 108
Franckowiak, A., Jean, P., Wood, M., Cheung, C. C., & Buson, S. 2018, A&A, 609, A210
Friedjung, M. 1987, A&A, 180, 155
Gallagher, J. S., & Ney, E. P. 1976, ApJ, 204, L35
Gallagher, J. S., Kaler, J. B., Olson, E. C., Hartkopf, W. I., & Hunter, D. A. 1980, PASP, 92, 46
Gehrz, R. D., Truran, J. W., Williams, R. E., & Starrfield, S. 1998, PASP, 110, 3
Gordon, A. C., Aydi, E., Page, K. L., et al. 2021, ApJ, 910, 134
Hachisu, I., & Kato, M. 2004, ApJL, 612, L57
Hachisu, I., & Kato, M. 2006, ApJS, 167, 59
Hachisu, I., & Kato, M. 2010, ApJ, 709, 680
Hachisu, I., & Kato, M. 2015, ApJ, 798, 76
Hachisu, I., & Kato, M. 2016, ApJ, 816, 26
Hachisu, I., & Kato, M. 2017, in The Golden Age of Cataclysmic Variables and Related Objects IV (Trieste: SISSA), 47, https://pos.sissa.it/cgi-bin/reader/conf.cgi?confid=315
Hachisu, I., & Kato, M. 2018a, ApJ, 858, 108
Hachisu, I., & Kato, M. 2018b, ApJS, 237, 4
Hachisu, I., & Kato, M. 2019a, ApJS, 241, 4
Hachisu, I., & Kato, M. 2019b, ApJS, 242, 18
Hachisu, I., & Kato, M. 2021, ApJS, 253, 27
Hachisu, I., Saio, H., Kato, M., Henze, M., & Shafter, A. W. 2020, ApJ, 902, 91
H.E.S.S. Collaboration 2022, Sci, 376, 77
Hopp, U. 1979, IBVS, 1633, 1
Izzo, L., Ederoclite, A., Della Valle, M., et al. 2012, MmSAI, 83, 830
Kahabka, P., & van den Heuvel, E. P. J. 1997, ARA&A, 35, 69
Kato, M., & Hachisu, I. 1994, ApJ, 437, 802
Kato, M. 1997, ApJS, 113, 121
Kato, M., & Hachisu, I. 2009, ApJ, 699, 1293
Kato, M., & Hachisu, I. 2011, ApJ, 743, 157
Kato, M., Hachisu, I., & Saio, H. 2017a, in The Golden Age of Cataclysmic Variables and Related Objects IV (Trieste: SISSA), 56, https://pos.sissa.it/cgi-bin/reader/conf.cgi?confid=315
Kato, M., Saio, H., & Hachisu, I. 2017b, ApJ, 838, 153
Kato, M., Saio, H., & Hachisu, I. 2022a, PASJ, 74, 1005
Kato, M., Saio, H., & Hachisu, I. 2022b, ApJL, 935, L15
König, O., Wilms, J., Arcodia, R., et al. 2022, Natur, 605, 248
Kolotilov, E. A. 1980, SvAL, 6, 268
Krautter, J., Oegelman, H., Starrfield, S., Wichmann, R., & Pfeffermann, E. 1996, ApJ, 456, 788
Li, K.-L., Metzger, B. D., Chomiuk, L., et al. 2017, NatAs, 1, 697
Li, K.-L., Hambsch, F.-J., Munari, U., et al. 2020, ApJ, 905, 114
Liszt, H. 2014, ApJ, 780, 10
Lloyd, H. M., O'Brien, T. J., Bode, M. F., et al. 1992, Natur, 356, 222
MAGIC Collaboration, Acciari, V. A., Ansoldi, S., et al. 2022, NatAs, 6, 689
Mallama, A. D., & Skillman, D. R. 1979, PASP, 91, 99
Martin, P., Dubus, G., Jean, P., Tatischeff, V., & Dosne, C. 2018, A&A, 612, A38
McLaughlin, D. B. 1942, ApJ, 95, 428
McLaughlin, D. B. 1943, Publications of the Observatory of the University of Michigan, 8 (Ann Arbor: Univ. Michigan Press), 149
McLaughlin, D. B. 1944, PA, 52, 109
Mclaughlin, D. B. 1960, in Stellar atmospheres, ed. J. L. Greenstein (Chicago: Univ. Chicago Press), 585
Metzger, B. D., Hascoët, R., Vurm, I., et al. 2014, MNRAS, 442, 713
Metzger, B. D., Finzell, T., Vurm, I., et al. 2015, MNRAS, 450, 2739
Mukai, K., & Ishida, M. 2001, ApJ, 551, 1024
Mukai, K., & Sokoloski, J. L. 2019, PhT, 11, 38
Munari, U., Hambsch, F.-J., & Frigo, A. 2017, MNRAS, 469, 4341
Nelson, T., Mukai, K., Li, K.-L., et al. 2019, ApJ, 872, 86
Ogelman, H., Orio, M., Krautter, J., & Starrfield, S. 1993, Natur, 361, 331
Orio, M., Parmar, A. N., Greiner, J., et al. 2002, MNRAS, 333, L11
Page, K. L., Osborne, J. P., Wagner, R. M., et al. 2013, ApJL, 768, L26
Page, K. L., Beardmore, A. P., & Osborne, J. P. 2020, AdSpR, 66, 1169
Payne-Gaposchkin, C. 1957, The Galactic Novae (Amsterdam: North-Holland)
Piccioni, A., Guarnieri, A., Bartolini, C., & Giovannelli, F. 1984, AcA, 34, 473
Prialnik, D. 1986, ApJ, 310, 222
Prialnik, D., & Kovetz, A. 1992, ApJ, 385, 665
Prialnik, D., & Kovetz, A. 1995, ApJ, 445, 789
Schaefer, B. E. 2018, MNRAS, 481, 3033
Schwarz, G. J., Ness, J.-U., Osborne, J. P., et al. 2011, ApJS, 197, 31
Shore, S. N., Starrfield, S., Ake III, T. B., & Hauschildt, P. H. 1997, ApJ, 490, 393
Skopal, A., Drechsel, H., Tarasova, T., et al. 2014, A&A, 569, A112
Sokolovsky, K. V., Mukai, K., Chomiuk, L., et al. 2020, MNRAS, 497, 2569

Sokolovsky, K. V., Li, K.-L., & Lopes de Oliveira, R. 2022, MNRAS, 514, 2239

Starrfield, S., Truran, J. W., Sparks, W. M., & Kutter, G. S. 1972, ApJ, 176, 169

Starrfield, S., Iliadis, C., Hix, W. R., Timmes, F. X., & Sparks, W. M. 2009, ApJ, 692, 1532

Tajitsu, A., Sadakane, K., Naito, H., et al. 2016, ApJ, 818, 191

Tanaka, J., Nogami, D., Fujii, M., et al. 2011, PASJ, 63, 911

Umeda, H., Nomoto, K., Yamaoka, H., & Wanajo, S. 1999, ApJ, 513, 861

Walter, F. M., Battisti, A., Towers, S. E., Bond, H. E., & Stringfellow, G. S. 2012, PASP, 124, 1057

Williams, R. E. 1992, AJ, 104, 725

Williams, R., Mason, E., Valle, M. D., & Ederoclite, A. 2008, ApJ, 685, 451

Williams, R., & Mason, E. 2010, Ap&SS, 327, 207

Williams, R. 2012, AJ, 144, 98

Vanlandingham, K. M., Schwarz, G. J., Shore, S. N., Starrfield, S., & Wagner, R. M. 2005, ApJ, 624, 914